Performance of the r^{2}SCAN functional in transition metal oxides

S. Swathilakshmi, Reshma Devi, and Gopalakrishnan Sai Gautam*

Department of Materials Engineering, Indian Institute of Science, Bengaluru, 560012, India

E-mail: saigautamg@iisc.ac.in

Crystal Structures

The crystal structures of all transition metal oxides (TMOs) considered in this work are displayed in Figure S1. CrO_2, MnO_2 and TiO_2 have a rutile ($P4_2/mnm$) ground state structure. In rutile, the metal ion forms a body-centred tetragonal lattice with six anions forming an octahedron around each metal ion while each anion is coordinated to three cations. These octahedra share edges to form chains along the c-axis, with distinct chains connected by shared corners.[1–5] TiO_2, CrO_2, and MnO_2 are diamagnetic, metallic ferromagnetic (FM),[3] and antiferromagnetic, (AFM)[6] respectively. VO_2, which exhibits a rutile structure at high temperatures, undergoes a transition to a monoclinic ($P2_1/c$) symmetry at temperatures below 341 K.[7] This structural transition is due to a metal-to-insulator transition (MIT), which causes the distance between V^{4+} to decrease, forming homopolar bonds, and trapping the d-electrons.[7] VO_2 exhibits a FM configuration.

Ti_2O_3 and Cr_2O_3 adopt a hexagonal ($R\bar{3}cR$) ground state symmetry with oxygen in hexagonal close packing and metal ions occupying two-thirds of the octahedral sites.[8,9] Cr_2O_3 exhibits a $\uparrow\downarrow\uparrow\downarrow$ magnetic configuration while Ti_2O_3 displays a $\uparrow\downarrow\downarrow\uparrow$ magnetic configuration on the transition metal (TM) centers along the a-axis.[10,11] V_2O_3 undergoes structural dis-

tortion from room temperature hexagonal ($R\bar{3}c$) with paramagnetic configuration to an AFM monoclinic ($I2/a$) form below 160-170 K due to a MIT.[12–14] The structural transition is associated with rotation of V-V bonds while the electrical transition is associated with an increase of V-V distance across the face shared octahedra. Fe_2O_3 exhibits hexagonal ($R\bar{3}c$) structure with oxygen forming a hexagonal close packed lattice and Fe^{3+} occupying two-thirds of the trigonally distorted octahedral sites. The AFM configuration of Fe_2O_3 is displayed in Figure S1.[15]

The rocksalt structures ($Fm\bar{3}m$) considered in this work include VO, MnO, FeO, CoO, and NiO, all of which adopt the type-II AFM configuration as their ground states.[16–21] To model the type-II AFM configuration, we used a $2 \times 2 \times 2$ supercell of the rocksalt rhombohedral primitive cell in VO, MnO, and FeO, while we used a $1 \times 2 \times 1$ supercell of the primitive for NiO and CoO.

The spinels considered in this study include Mn_3O_4, Fe_3O_4, and Co_3O_4. Among the spinels, Mn_3O_4 is tetragonally distorted ($I41/amd$) due to the Jahn-Teller distortion of the Mn^{3+} present in the octahedral sites of the structure.[22] Also, we consider the "FIM6" ferrimagnetic configuration since it was reported to be the most stable among the 6 different ferrimagnetic configurations in our previous work.[23] At room temperature, Fe_3O_4 exhibits an inverse cubic spinel ($Fd\bar{3}m$) with O atoms forming cubic close packed array, Fe^{3+} occupying the tetrahedral sites, and both Fe^{3+} and Fe^{2+} randomly distributed in the octahedral sites. Additionally, Fe_3O_4 is reported to exhibit a Verway transition away from its room temperature cubic structure to either an orthorhombic[24] or a monoclinic[25] structure upon relaxation at low temperatures (< 120 K). This results in charge ordering of the Fe^{2+} and Fe^{3+} in the octahedral sites[26] and an opening of the band gap.[27] Co_3O_4 exhibits the primitive spinel structure ($Fd\bar{3}m$) with Co^{2+} occupying tetrahedral sites in high spin state in an AFM configuration while Co^{3+} occupy octahedral sites in their low spin, diamagnetic state.[28–30]

We consider FM-ordered α-Mn_2O_3 with the bixbyite structure similar to our previous work,[23] wherein each Mn^{3+} ions are octahedrally coordinated with O while each O atom is

surrounded by 4 Mn atoms. Below 300 K, Mn_2O_3 exhibits Jahn-Teller distortion from cubic to an orthorhombic form ($Pbca$).[31] $LiNiO_2$ possesses a layered structure with an alternating layer of Li and Ni atoms,[32] and we used a primitive cell of $LiNiO_2$ ($P1m1$) in our calculations. V_2O_5 exhibits an orthorhombic ($Pmmn$) structure, and adopts a layered morphology with each oxygen coordinated vanadium (i.e., VO_5 square pyramids) sharing edges and corners.[33]

CuO exhibits a monoclinic ($C2/c$) ground state with AFM configuration where each oxygen atom is surrounded by a distorted copper tetrahedron while each copper atom is surrounded by four oxygen in a square-planar configuration.[34] We used a $2 \times 1 \times 2$ supercell to model the AFM ground state of CuO. In Cu_2O, oxygen forms a BCC lattice with each oxygen ion surrounded by a tetrahedron of copper ions while copper is coordinated with two oxygens and thus exhibits a linear O-Cu-O configuration.[34,35]

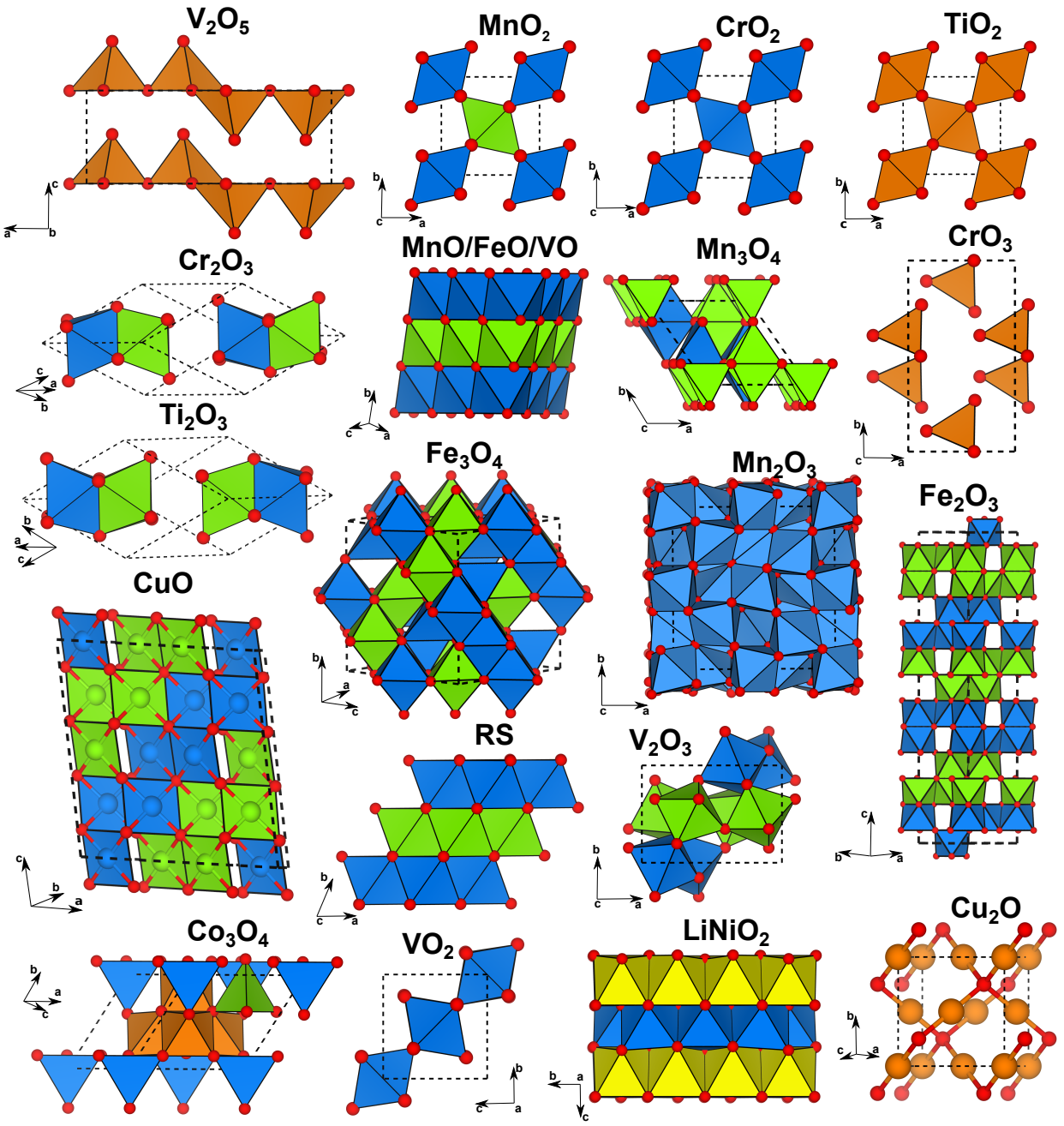

Figure S1: Crystal structures of TMOs considered in our work. Blue, green, and orange polyhedra represent TM centers with up, down, and no spin, respectively. Red spheres are oxygen atoms. Yellow polyhedra in $LiNiO_2$ represent Li atoms. RS refers to the $1 \times 2 \times 1$ supercell of the rocksalt structure of NiO and CoO.

Oxidation energetics of Cr and Cu oxides

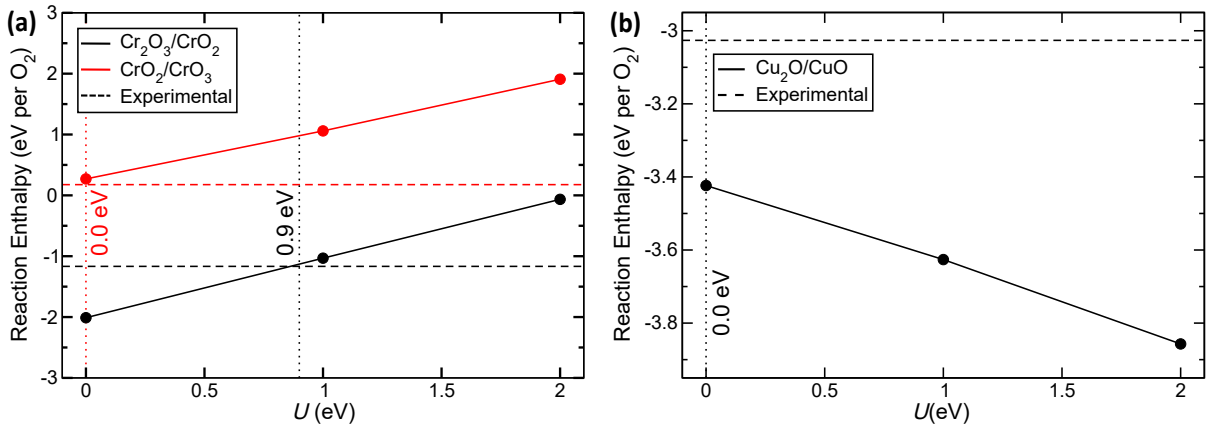

Figure S2: Oxidation enthalpy versus applied U within the restored regularized strongly constrained and appropriately normed (r^{2}SCAN)+U framework for (a) Cr and (b) Cu oxides. Notations on the plot are similar to those used in Figure 1 of the main text.

On-site magnetic moments

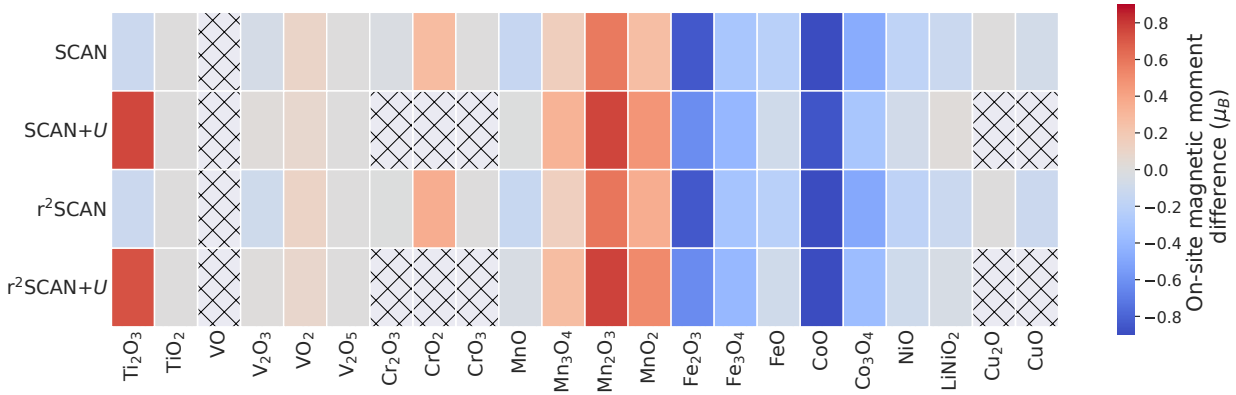

Figure S3: Difference between experimental and calculated on-site magnetic moments using the four functionals, plotted as a heatmap, for various systems. Red (blue) squares indicate overestimated (underestimated) calculated lattice volumes versus experiment.

Transferability checks

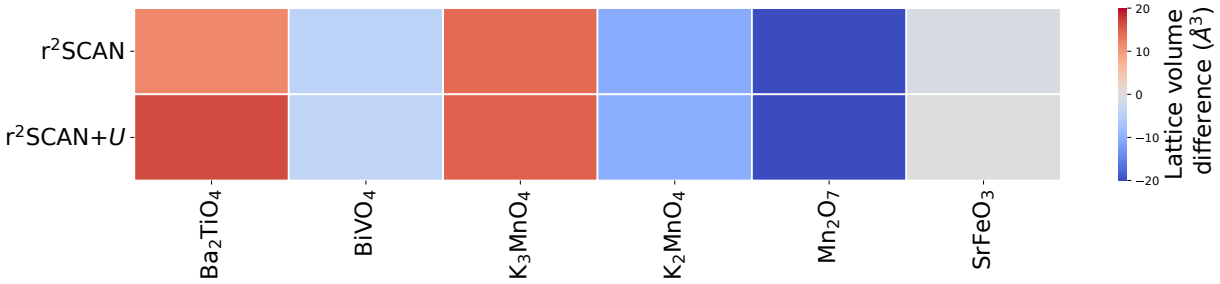

Figure S4: Difference between experimental and calculated lattice volumes (using r^{2}SCAN and r^{2}SCAN+U), plotted as a heatmap, for various systems. Red (blue) squares indicate overestimated (underestimated) calculated lattice volumes versus experiment.

Table S1: Optimal U value for all the TMs obtained for the strongly constrained and appropriately normed (SCAN)+U functional used from previous study.[23,36]

Element	Optimal U (eV)
Ti	2.5
V	1.0
Cr	0.0
Mn	2.7
Fe	3.1
Co	3.0
Ni	2.5
Cu	0.0

Lattice parameters, on-site magnetic moments, and band gaps

Table S2: Lattice parameters, on-site magnetic moments, and band gaps obtained from experiments (denoted by 'Expt.') and calculated by SCAN, SCAN+U, r^{2}SCAN, and r^{2}SCAN+U for all TMOs considered in this study. The U values used with r^{2}SCAN+U and SCAN+U are the corresponding optimal U values obtained for each TM, i.e., from Figure 1 of the main text and Table S1, respectively.

Composition	Source	Lattice constants (Å)			Lattice angles (°)			On-site Magnetic	Band gap
(space group)		a	b	c	α	β	γ	moment (μ_B)	(eV)
Ti_2O_3	Expt.	5.43	5.43	5.43	56.7	56.7	56.7	0.03-0.20 [11,37]	0.20 [38]
($R\bar{3}cR$)									
	SCAN	5.45	5.45	5.45	55.8	55.8	55.8	0.002	Metallic
	SCAN+U	5.57	5.61	5.57	55.8	55.9	55.8	0.872	1.54
	r^{2}SCAN	5.46	5.46	5.46	55.7	55.7	55.7	0.002	Metallic
	r^{2}SCAN+U	5.49	5.49	5.49	57.5	57.5	57.5	0.839	1.28
TiO_2	Expt.	4.59	4.59	2.96	90.0	90.0	90.0	0	3.00 [39]
($P4_2/mnm$)									
	SCAN	4.60	4.60	2.96	90.0	90.0	90.0	0	1.95
	SCAN+U	4.61	4.61	3.00	90.0	90.0	90.0	0	2.21
	r^{2}SCAN	4.60	4.60	2.96	90.0	90.0	90.0	0	1.94
	r^{2}SCAN+U	4.62	4.62	2.99	90.0	90.0	90.0	0	2.21
VO	Expt.	5.83	5.83	5.83	60.0	60.0	60.0	N/A	N/A
($Fm\bar{3}m$)	SCAN	6.31	6.31	5.84	57.3	57.3	60.0	2.451	1.63
	SCAN+U	6.31	6.31	5.94	57.9	57.9	60.0	2.564	2.12
	r^{2}SCAN	6.32	6.32	5.83	57.2	57.2	60.0	2.443	1.37
	r^{2}SCAN+U	6.33	6.33	5.92	57.7	57.7	60.0	2.554	2.04

Continued on next page

Table S2: Lattice parameters, on-site magnetic moments, and band gaps obtained from experiments (denoted by 'Expt.') and calculated by SCAN, SCAN+U, r^{2}SCAN, and r^{2}SCAN+U for all TMOs considered in this study. The U values used with r^{2}SCAN+U and SCAN+U are the corresponding optimal U values obtained for each TM, i.e., from Figure 1 of the main text and Table S1, respectively. (Continued)

V_2O_3	Expt.	7.26	5.00	5.55	90.0	96.8	90.0	1.20-2.37	0.20
($I2/a$)								[40,41]	[42]
	SCAN	7.23	5.03	5.56	90.0	96.8	90.0	1.728	Metallic
	SCAN+U	7.28	5.10	5.55	90.0	96.4	90.0	1.804	0.73
	r^{2}SCAN	7.29	5.01	5.52	90.0	97.5	90.0	1.690	Metallic
	r^{2}SCAN+U	7.29	5.09	5.56	90.0	96.4	90.0	1.795	0.36
VO_2	Expt.	5.57	4.54	5.38	90.0	122.6	90.0	∼1.00	0.70
($P21/c$)								[43]	[42]
	SCAN	5.68	4.54	5.35	90.0	122.1	90.0	1.105	Metallic
	SCAN+U	5.83	4.52	5.35	90.0	122.3	90.0	1.074	Metallic
	r^{2}SCAN	5.69	4.55	5.36	90.0	122.1	90.0	1.111	Metallic
	r^{2}SCAN+U	5.83	4.53	5.36	90.0	122.3	90.0	1.082	Metallic
V_2O_5	Expt.	11.54	3.57	4.38	90.0	90.0	90.0	0	2.50
($Pmmn$)									[44]
	SCAN	11.56	3.55	4.28	90.0	90.0	90.0	0	1.69
	SCAN+U	11.57	3.56	4.28	90.0	90.0	90.0	0	1.80
	r^{2}SCAN	11.60	3.55	4.32	90.0	90.0	90.0	0	1.72
	r^{2}SCAN+U	11.59	3.57	4.30	90.0	90.0	90.0	0	1.81
Cr_2O_3	Expt.	5.36	5.36	5.36	55.1	55.1	55.1	± 2.760	3.20
($R\bar{3}cR$)								[45]	[46]
	SCAN	5.36	5.36	5.36	55.0	55.0	55.0	2.736	1.89
	r^{2}SCAN	5.38	5.38	5.38	54.8	54.8	54.8	2.755	1.71
CrO_2	Expt.	4.42	4.42	2.92	90.0	90.0	90.0	2.00	Metallic

Continued on next page

Table S2: Lattice parameters, on-site magnetic moments, and band gaps obtained from experiments (denoted by 'Expt.') and calculated by SCAN, SCAN+U, r^{2}SCAN, and r^{2}SCAN+U for all TMOs considered in this study. The U values used with r^{2}SCAN+U and SCAN+U are the corresponding optimal U values obtained for each TM, i.e., from Figure 1 of the main text and Table S1, respectively. (Continued)

($P4_2/mnm$)								[3]	[3]
	SCAN	4.40	4.40	2.91	90.0	90.0	90.0	2.278	Metallic
	r^{2}SCAN	4.41	4.41	2.92	90.0	90.0	90.0	2.356	Metallic
CrO_3	Expt.	4.79	8.56	5.74	90.0	90.0	90.0	0	3.80[47]
($C2cm$)	SCAN	4.68	8.52	5.70	90.0	90.0	90.0	0	1.89
	r^{2}SCAN	4.75	8.59	5.72	90.0	90.0	90.0	0	1.95
MnO	Expt.	6.29	6.29	6.29	60.0	60.0	60.0	4.580	3.60-3.80
($Fm\bar{3}m$)								[48]	[49]
	SCAN	6.29	6.29	6.17	59.4	59.4	60.0	4.436	1.39
	SCAN+U	6.31	6.31	6.24	59.6	59.6	60.0	4.576	1.97
	r^{2}SCAN	6.30	6.30	6.19	59.4	59.4	60.0	4.446	1.45
	r^{2}SCAN+U	6.32	6.32	6.24	59.6	59.6	60.0	4.542	1.85
Mn_3O_4	Expt.	5.75	6.22	5.75	117.5	90.0	117.5	4.34,3.25-3.64	2.30-2.50
($I4_1/amd$)								[50]	[51]
	SCAN	5.75	6.19	5.75	117.4	90.5	117.4	3.638,4.383	0.96
	SCAN+U	5.80	6.23	5.80	117.5	90.5	117.5	3.814,4.556	1.38
	r^{2}SCAN	5.76	6.21	5.76	117.4	90.5	117.4	3.683,4.375	0.80
	r^{2}SCAN+U	5.80	6.24	5.80	117.5	90.4	117.5	3.807,4.504	1.06
Mn_2O_3	Expt.	9.41	9.42	9.40	90.0	90.0	90.0	3.10-4.20	1.20-1.29
($Pbca$)								[31,52]	[53,54]
	SCAN	9.40	9.42	9.41	90.0	90.0	90.0	3.681-3.799	Metallic
	SCAN+U	9.45	9.48	9.47	90.0	90.0	90.0	3.864-3.923	0.24
	r^{2}SCAN	9.42	9.43	9.43	90.0	90.0	90.0	3.696-3.849	Metallic

Continued on next page

Table S2: Lattice parameters, on-site magnetic moments, and band gaps obtained from experiments (denoted by 'Expt.') and calculated by SCAN, SCAN+U, r^{2}SCAN, and r^{2}SCAN+U for all TMOs considered in this study. The U values used with r^{2}SCAN+U and SCAN+U are the corresponding optimal U values obtained for each TM, i.e., from Figure 1 of the main text and Table S1, respectively. (Continued)

	r^{2}SCAN+U	9.46	9.48	9.49	90.0	90.0	90.0	3.872-3.926	Metallic
MnO_2	Expt.	4.40	4.40	2.87	90.0	90.0	90.0	2.350	0.27-0.3
($P4_2/mnm$)								[6]	[55,56]
	SCAN	4.39	4.39	2.85	90.0	90.0	90.0	2.612	0.32
	SCAN+U	4.40	4.40	2.88	90.0	90.0	90.0	2.821	0.66
	r^{2}SCAN	4.39	4.39	2.87	90.0	90.0	90.0	2.704	0.11
	r^{2}SCAN+U	4.40	4.40	2.89	90.0	90.0	90.0	2.868	0.40
FeO	Expt.	6.08	6.08	6.08	60.0	60.0	60.0	3.32-4.20	2.40
($Fm\bar{3}m$)								[57,58]	[59]
	SCAN	5.85	5.97	6.25	61.4	60.4	59.3	3.542	0.17
	SCAN+U	6.14	6.14	6.02	61.4	61.4	59.6	3.669	1.58
	r^{2}SCAN	5.97	5.88	6.13	61.4	62.4	60.6	3.542	0.14
	r^{2}SCAN+U	6.14	6.13	6.13	60.3	59.6	60.1	3.675	1.47
Fe_3O_4	Expt.	8.39	8.39	8.39	90.0	90.0	90.0	4.44,4.10	0.14
($Fd\bar{3}m$)								[60]	[27]
	SCAN	8.34	8.34	8.34	90.0	90.0	90.0	3.793,3.844	Metallic
	SCAN+U	8.40	8.40	8.46	90.0	90.0	90.3	3.694,4.172	0.47
	r^{2}SCAN	8.36	8.36	8.36	90.2	89.5	89.4	3.782,3.839	Metallic
	r^{2}SCAN+U	8.41	8.41	8.48	90.0	90.0	90.3	3.706,4.161	0.42
Fe_2O_3	Expt.	5.04	5.04	27.54	90.0	90.0	120.0	4.90	2.20
($R\bar{3}c$)								[61]	[62]
	SCAN	5.03	5.03	27.49	90.0	90.0	120.0	4.056	0.60
	SCAN+U	5.06	5.06	27.50	90.0	90.0	120.0	4.278	1.83

Continued on next page

Table S2: Lattice parameters, on-site magnetic moments, and band gaps obtained from experiments (denoted by 'Expt.') and calculated by SCAN, SCAN+U, r^{2}SCAN, and r^{2}SCAN+U for all TMOs considered in this study. The U values used with r^{2}SCAN+U and SCAN+U are the corresponding optimal U values obtained for each TM, i.e., from Figure 1 of the main text and Table S1, respectively. (Continued)

	r^{2}SCAN	5.05	5.05	27.52	90.0	90.0	120.0	4.052	0.61
	r^{2}SCAN+U	5.06	5.06	27.55	90.0	90.0	120.0	4.269	1.85
CoO	Expt.	3.01	6.01	3.01	60.0	60.0	60.0	± 3.35-3.80 [58,63]	2.40 [64,65]
($Fm\bar{3}m$)									
	SCAN	3.00	5.99	3.00	59.9	60.0	60.0	2.581	0.91
	SCAN+U	3.02	6.00	3.02	59.8	60.0	59.9	2.717	2.64
	r^{2}SCAN	2.99	5.99	2.99	60.0	60.0	60.0	2.575	0.61
	r^{2}SCAN+U	3.01	6.00	3.01	59.9	60.0	59.9	2.668	1.98
Co_3O_4	Expt.	5.71	5.71	5.71	60.0	60.0	60.0	± 3.02,0.00 [30]	1.60 [64]
($Fd\bar{3}m$)									
	SCAN	5.69	5.69	5.69	60.0	60.0	60.0	2.549	1.20
	SCAN+U	5.71	5.71	5.71	60.0	60.0	60.0	2.716	1.23
	r^{2}SCAN	5.69	5.69	5.69	60.0	60.0	60.0	2.530	0.81
	r^{2}SCAN+U	5.71	5.71	5.71	60.0	60.0	60.0	2.653	0.83
NiO	Expt.	2.95	5.91	2.95	60.0	60.0	60.0	± 1.64-1.90 [48,66]	4.30 [67]
($Fm\bar{3}m$)									
	SCAN	2.94	5.87	2.94	60.0	60.0	60.0	1.585	2.39
	SCAN+U	2.95	5.89	2.95	60.0	60.0	60.0	1.690	3.35
	r^{2}SCAN	2.94	5.87	2.94	60.0	60.0	60.0	1.577	2.11
	r^{2}SCAN+U	2.94	5.89	2.94	60.0	60.0	60.0	1.677	3.17
$LiNiO_2$	Expt.	5.01	5.01	5.02	80.4	70.6	60.0	1.00 [68,69]	N/A
($P1m1$)									
	SCAN	5.11	4.87	5.06	78.5	67.7	58.3	0.879	Metallic

Continued on next page

Table S2: Lattice parameters, on-site magnetic moments, and band gaps obtained from experiments (denoted by 'Expt.') and calculated by SCAN, SCAN+U, r^{2}SCAN, and r^{2}SCAN+U for all TMOs considered in this study. The U values used with r^{2}SCAN+U and SCAN+U are the corresponding optimal U values obtained for each TM, i.e., from Figure 1 of the main text and Table S1, respectively. (Continued)

	SCAN+U	5.10	4.87	5.07	78.6	67.3	58.4	1.020	0.13
	r^{2}SCAN	4.97	4.94	4.99	80.2	70.2	59.8	0.877	Metallic
	r^{2}SCAN+U	5.10	4.87	5.07	78.6	67.8	58.4	0.956	0.08
Cu_2O	Expt.	4.27	4.27	4.27	90.0	90.0	90.0	0	2.17-2.4
($Pn\bar{3}m$)									[34,70]
	SCAN	4.23	4.23	4.23	90.0	90.0	90.0	0	0.60
	r^{2}SCAN	4.23	4.23	4.23	90.0	90.0	90.0	0	0.58
CuO	Expt.	9.37	3.42	10.26	90.0	99.5	90.0	0.680	1.40
($C2/c$)								[71]	[34]
	SCAN	8.80	3.70	10.26	90.0	96.3	90.0	0.607	0.79
	r^{2}SCAN	8.67	3.79	10.27	90.0	96.1	90.0	0.566	0.46

Table S3: Lattice parameters reported experimentally (denoted by 'Expt.') and calculated by r^{2}SCAN, and r^{2}SCAN+U for all TMOs considered as transferability checks. The U values used with r^{2}SCAN+U are the corresponding optimal U values obtained for each TM (from Figure 1 of the main text).

Composition (space group)	Source	Lattice constants (Å)			Lattice angles (°)		
		a	b	c	α	β	γ
Ba_2TiO_4	Expt.	6.09	7.68	10.54	90.0	93.0	90.0
($P2_1/n$)	r^{2}SCAN	6.17	7.73	10.60	90.0	93.6	90.0
	r^{2}SCAN+U	6.20	7.75	10.63	90.0	93.9	90.0
$BiVO_4$	Expt.	5.19	5.09	11.69	90.0	90.0	90.4
($I2/b$)	r^{2}SCAN	5.13	5.13	11.59	90.0	90.0	90.0
	r^{2}SCAN+U	5.13	5.13	11.58	90.0	90.0	90.0
K_3MnO_4	Expt.	5.90	5.90	8.01	90.0	90.0	90.0
($I\bar{4}2m$)	r^{2}SCAN	6.51	6.50	6.92	90.0	90.0	90.0
	r^{2}SCAN+U	6.50	6.50	6.94	90.0	90.0	90.0
K_2MnO_4	Expt.	7.67	5.90	10.36	90.0	90.0	90.0
($Pnma$)	r^{2}SCAN	7.64	5.81	10.32	90.0	90.0	90.0
	r^{2}SCAN+U	7.64	5.81	10.32	90.0	90.0	90.0
Mn_2O_7	Expt.	6.80	16.69	9.45	90.0	100.2	90.0
($P2_1/c$)	r^{2}SCAN	6.72	16.68	9.20	90.0	99.5	90.0
	r^{2}SCAN+U	6.73	16.66	9.19	90.0	99.5	90.0
$SrFeO_3$	Expt.	3.85	3.85	3.85	90.0	90.0	90.0
($Pm\bar{3}m$)	r^{2}SCAN	3.83	3.83	3.83	90.0	90.0	90.0
	r^{2}SCAN+U	3.85	3.85	3.85	90.0	90.0	90.0

Computational time

Computational time required per ionic step for a TMO is calculated by dividing the overall computational time by the total number of ionic steps completed during its structural relaxation. Similarly, computational time required per electronic step for a TMO is calculated by dividing the overall computational time by the total number of electronic steps completed during its structural relaxation. Relative computational time is subsequently calculated as the computational time (overall, per ionic step, or per electronic step) of a given functional divided by the corresponding computational time (overall, per ionic step, or per electronic step) taken by the SCAN functional. Thus a value of 1.0 on the computational time scale indicates that the functional takes an identical amount of time for structure relaxation as SCAN, while values lower (greater) than 1.0 indicate lower (greater) computational time than SCAN. For a given TM-O_2 binary system, we simply averaged the relative computational times across the individual TMOs constituting the binary system. All computational times were normalized per number of computing cores used in a calculation.

Density of states

The electronic density of states (DOS) for all TMOs not illustrated in Figure 2 of the main text are included in this section, from Figures S5 to S21. In each DOS plot, solid orange lines correspond to the $2p$-states of O, while solid green lines indicate the $3d$-states of the TM. Li s states are not displayed in Figure S20. The dashed black line represents the Fermi level. The dotted vertical lines represent the valence and conduction band edges. Magnitude of the band gap in all gapped systems is indicated by the text annotation next to the conduction band minimum. The zero on the energy scale is set to the valence band maximum for TMOs with a finite band gap and to the Fermi level in metallic systems.

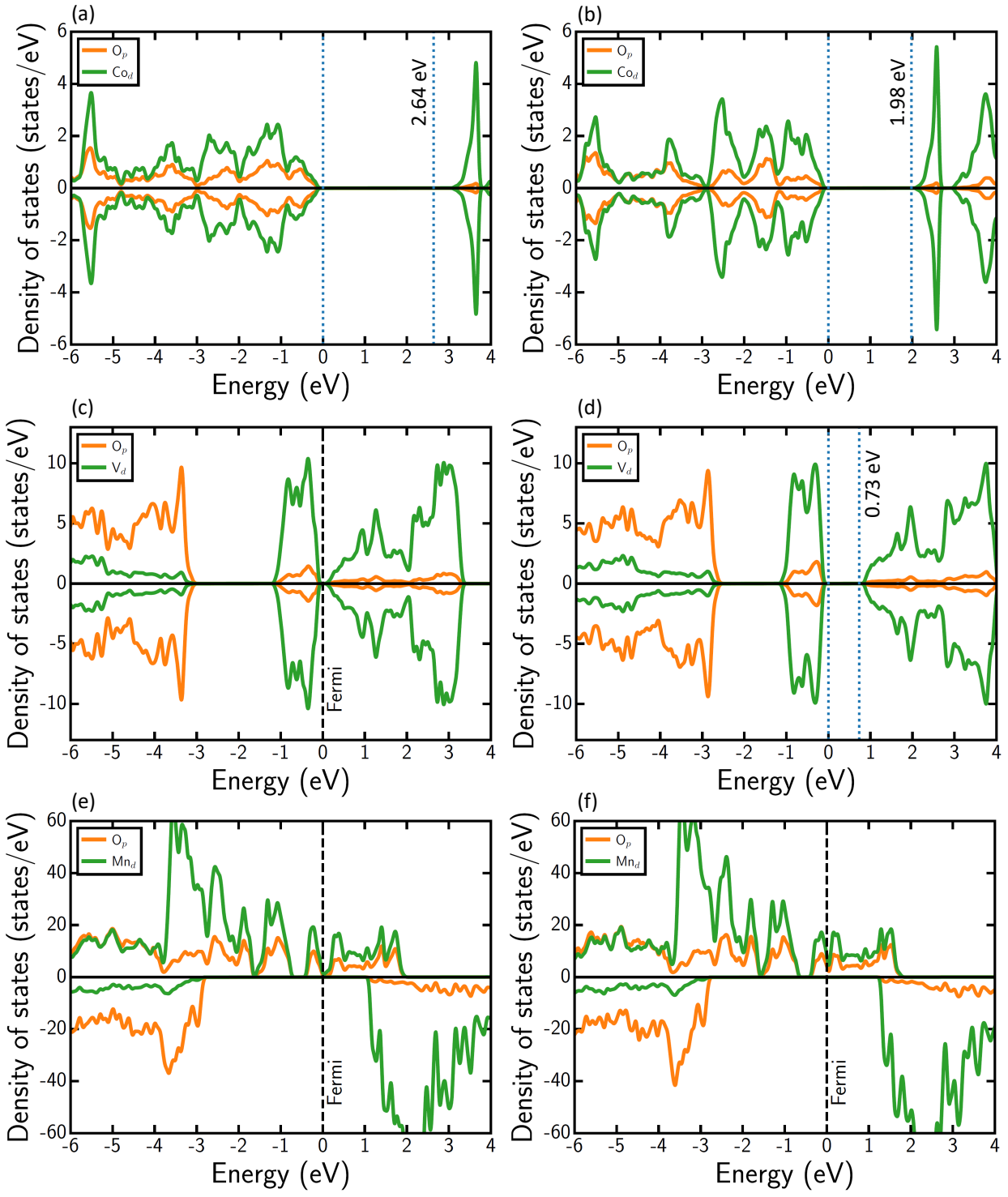

Figure S5: DOS plots for CoO calculated using (a) SCAN+U, and (b) r^{2}SCAN+U. DOS plots for V_2O_3 calculated using (c) SCAN, and (d) SCAN+U. DOS plots for Mn_2O_3 calculated using (e) SCAN and (f) r^{2}SCAN.

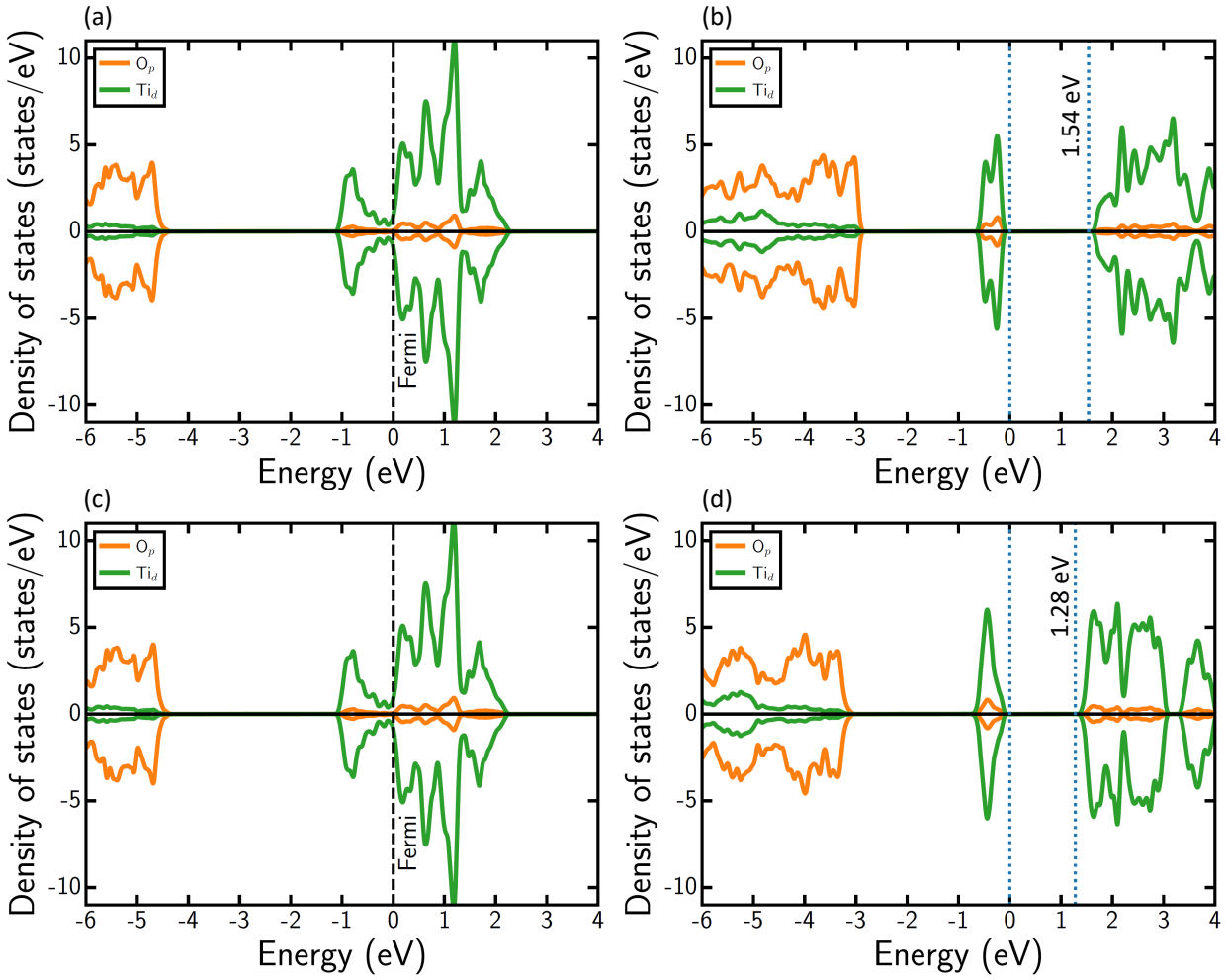

Figure S6: DOS plots for Ti_2O_3 calculated using (a) SCAN, (b) SCAN+U, (c) r^{2}SCAN and (d) r^{2}SCAN+U.

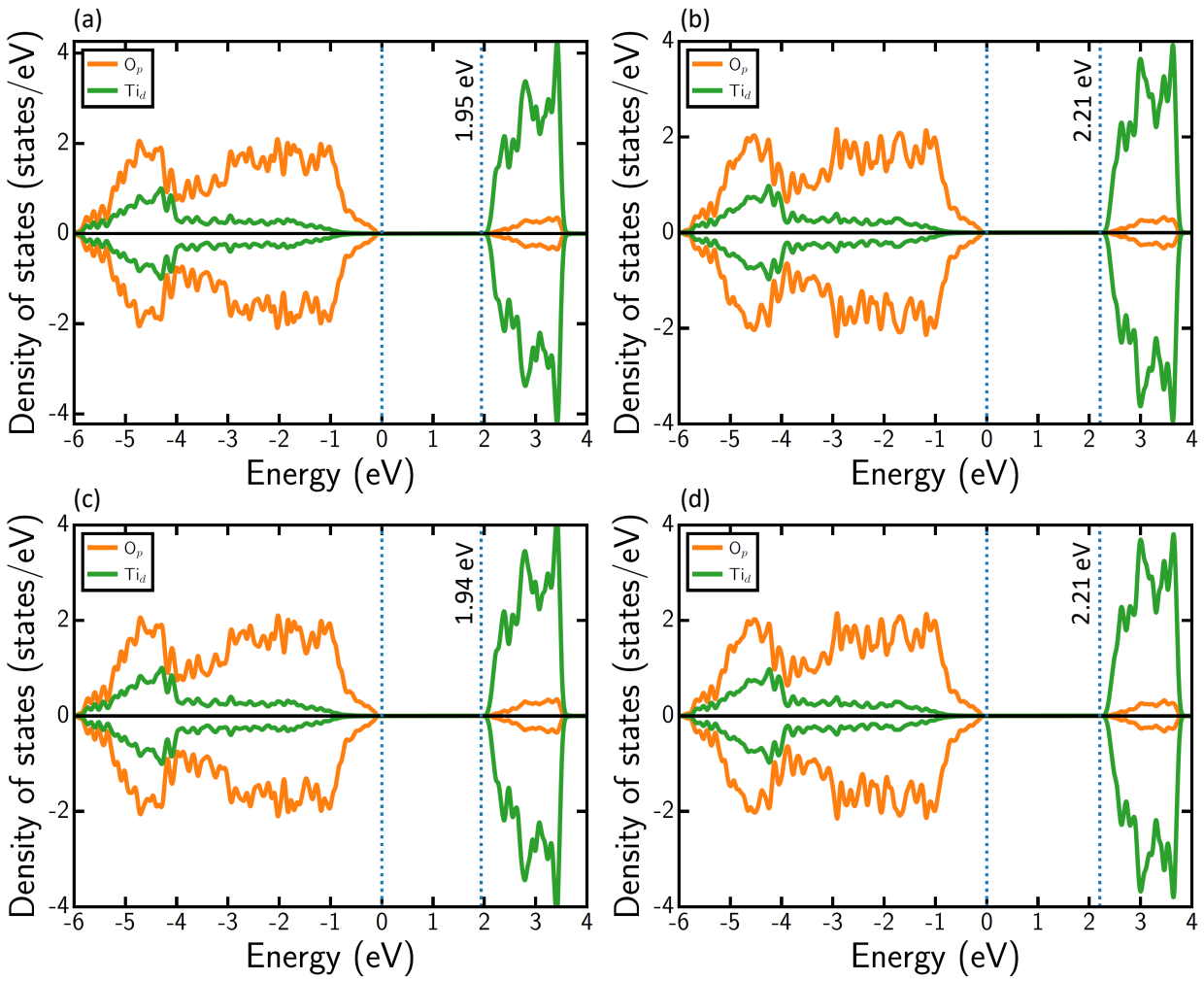

Figure S7: DOS plots for TiO_2 calculated using (a) SCAN, (b) SCAN+U, (c) r^{2}SCAN and (d) r^{2}SCAN+U.

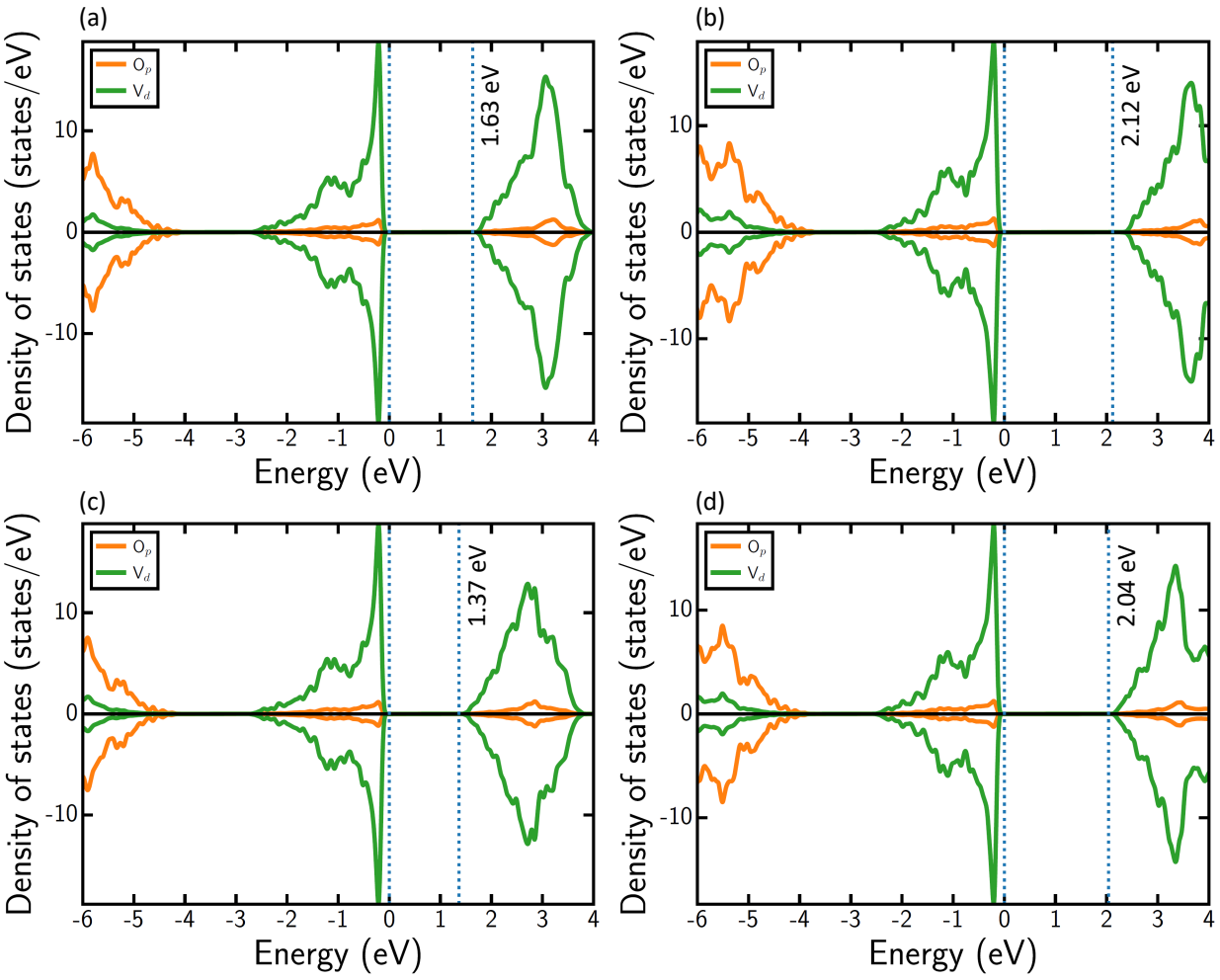

Figure S8: DOS plots for VO calculated using (a) SCAN, (b) SCAN+U, (c) r^{2}SCAN and (d) r^{2}SCAN+U.

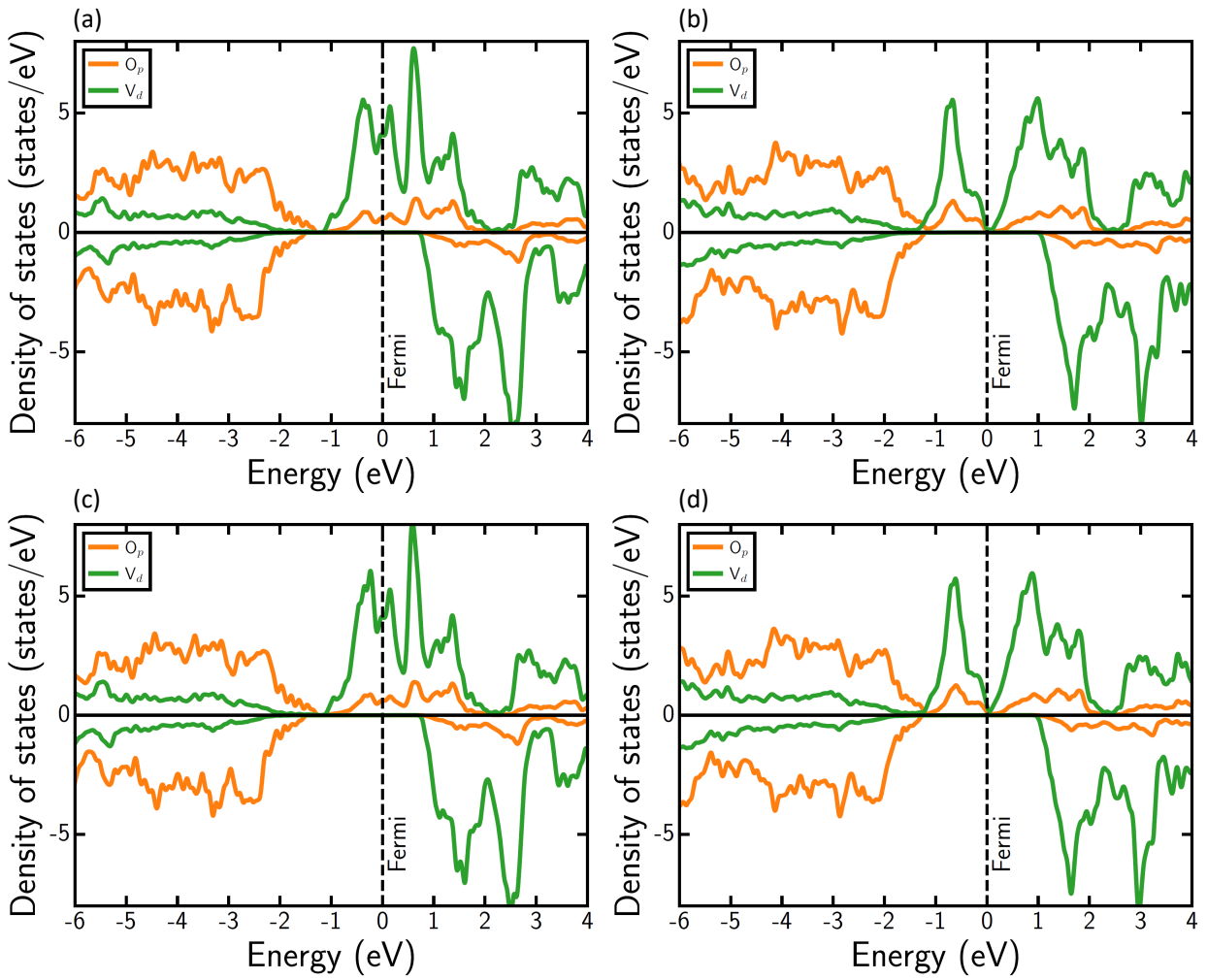

Figure S9: DOS plots for VO_2 calculated using (a) SCAN, (b) SCAN+U, (c) r^{2}SCAN and (d) r^{2}SCAN+U.

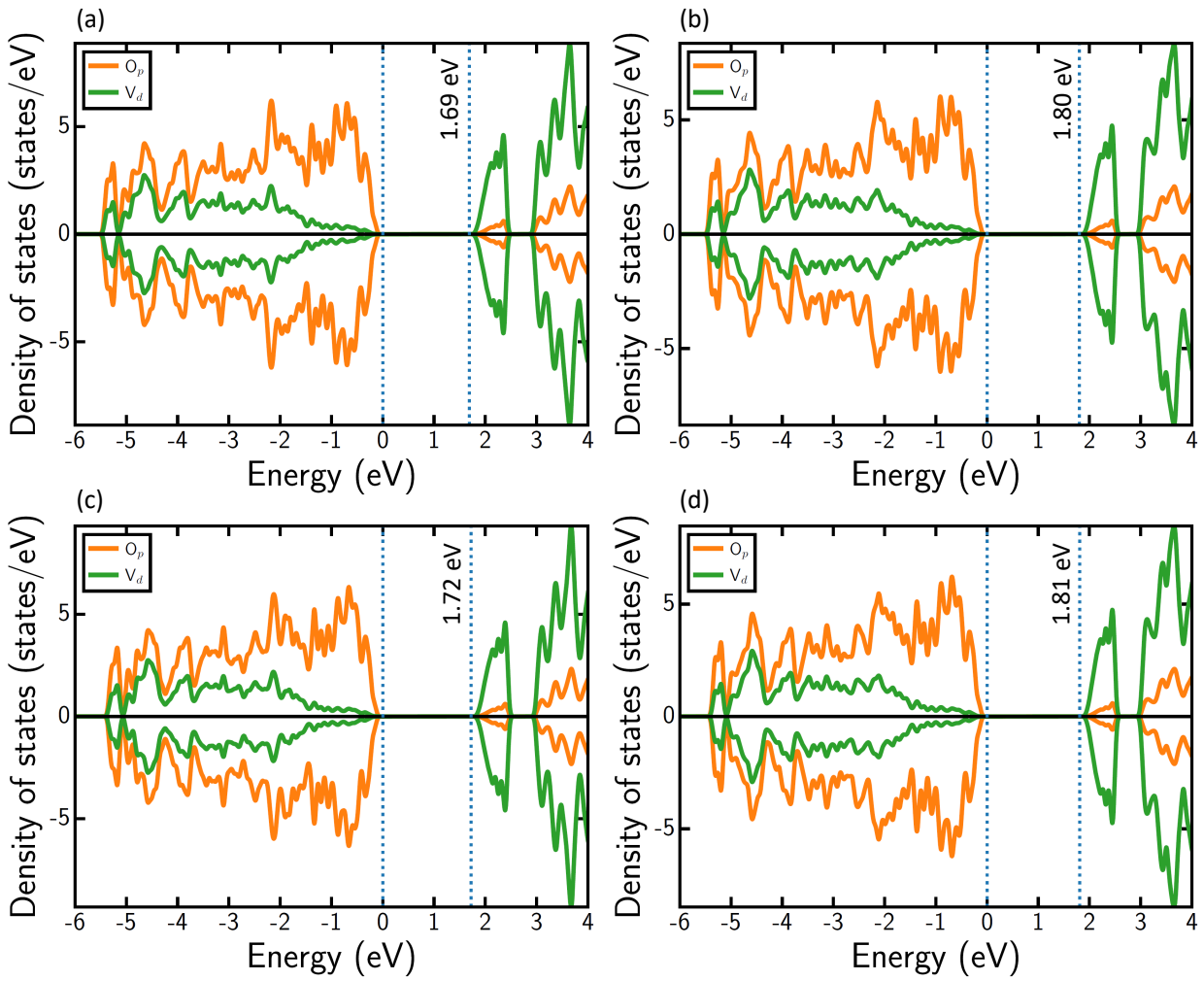

Figure S10: DOS plots for V_2O_5 calculated using (a) SCAN, (b) SCAN+U, (c) r^{2}SCAN and (d) r^{2}SCAN+U.

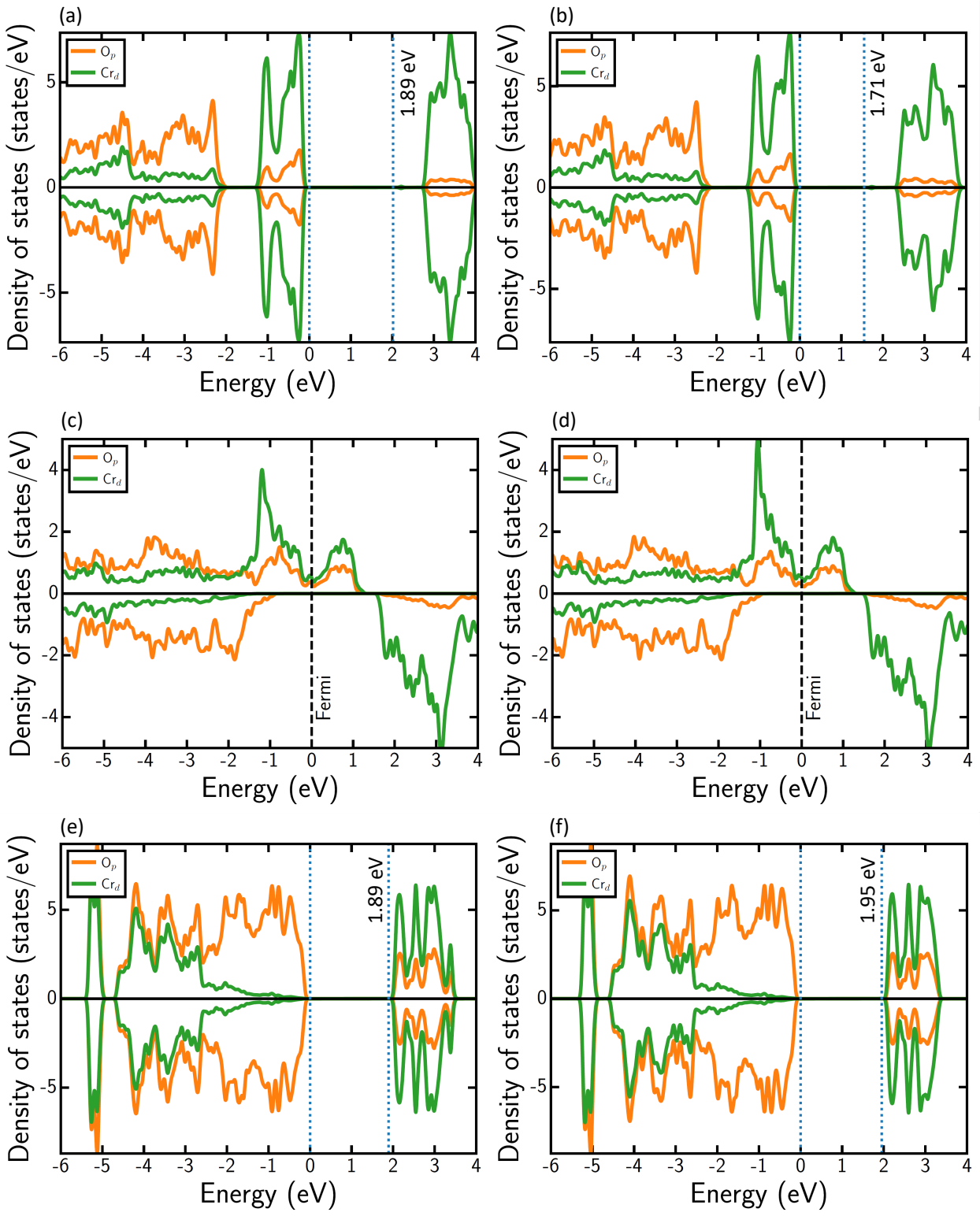

Figure S11: DOS plots for Cr_2O_3 (panels a and b), CrO_2 (c and d), and CrO_3 (e and f), calculated using SCAN (panels a, c, and e) and r^{2}SCAN (b, d, and f).

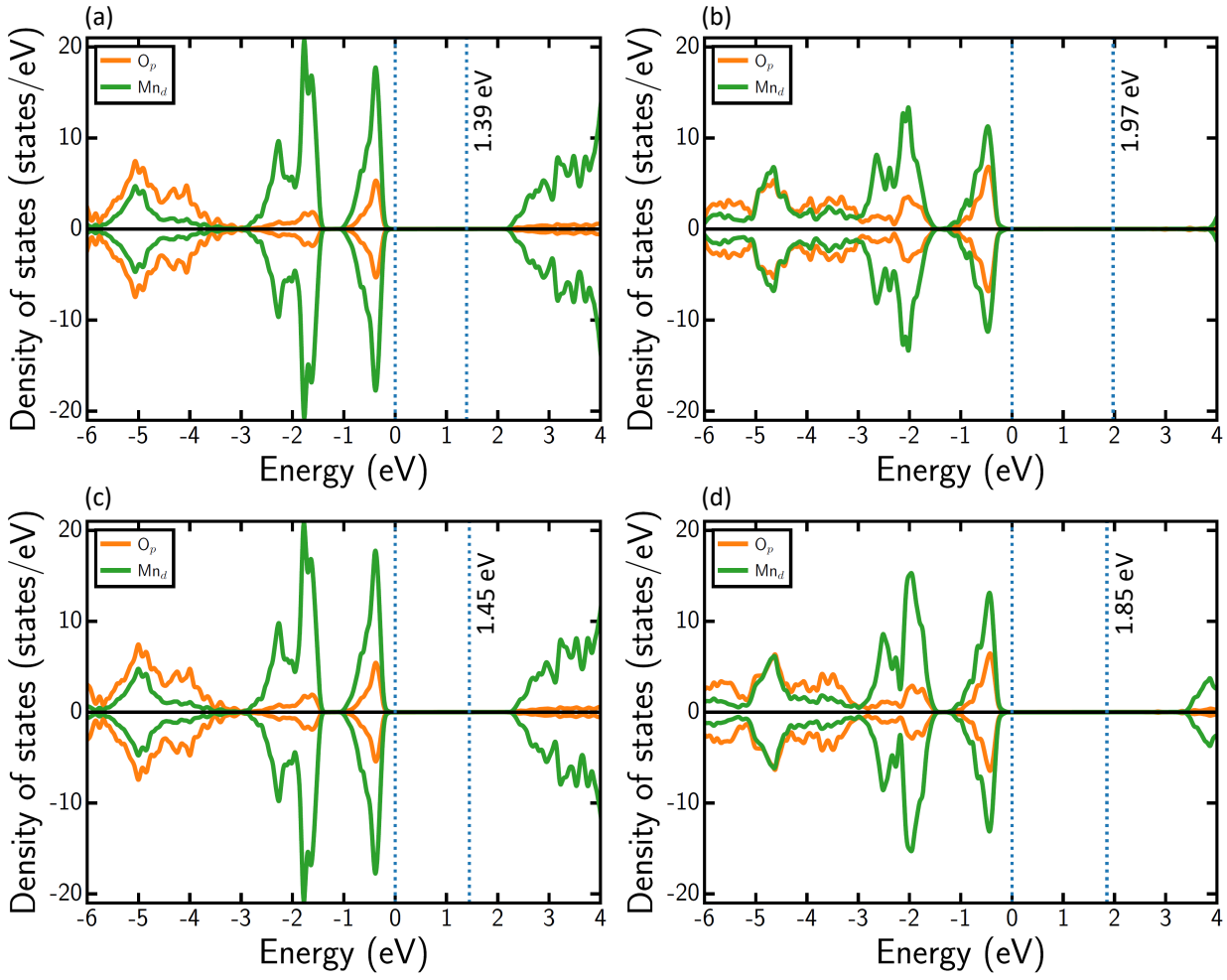

Figure S12: DOS plots for MnO calculated using (a) SCAN, (b) SCAN+U, (c) r^{2}SCAN and (d) r^{2}SCAN+U.

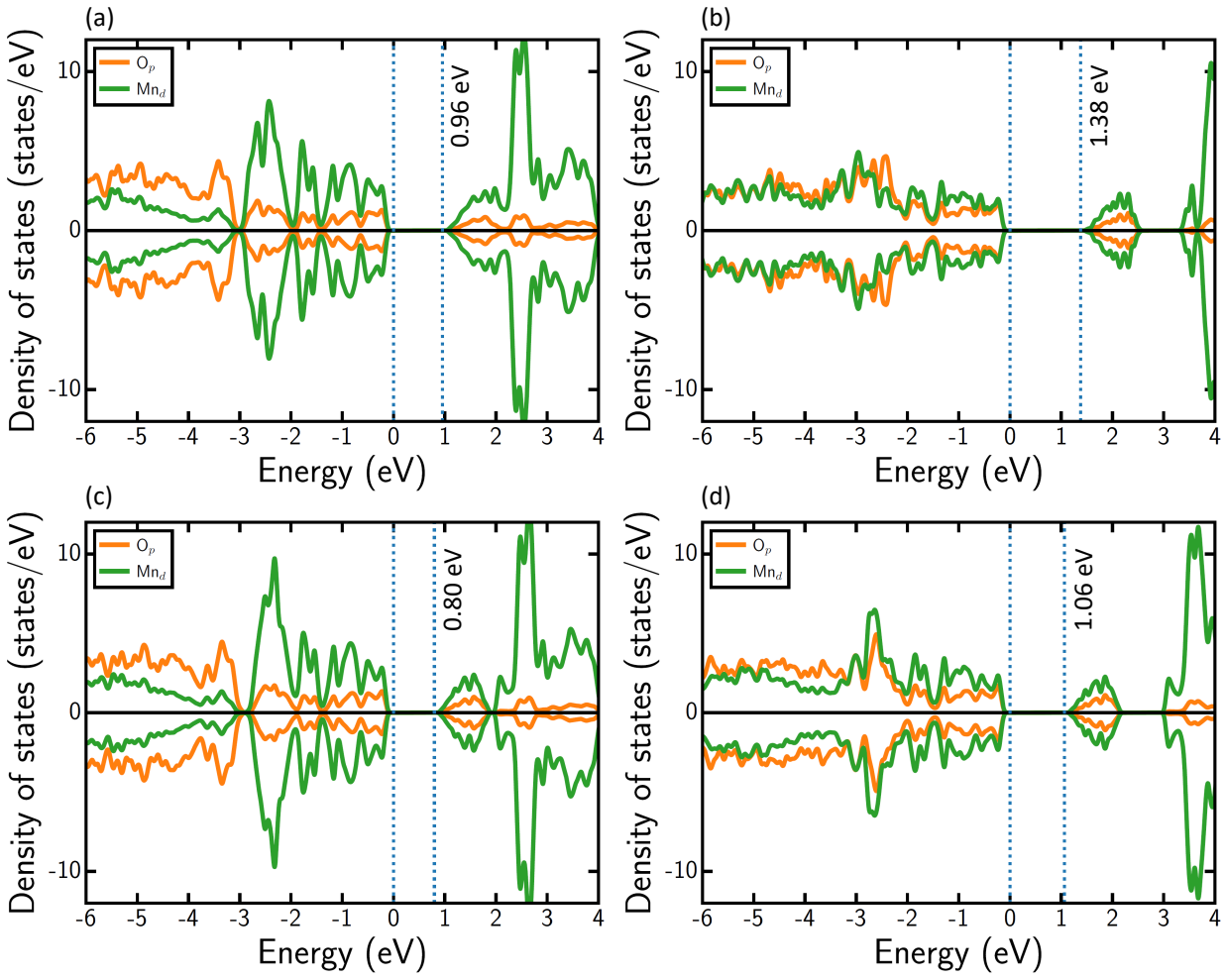

Figure S13: DOS plots for Mn_3O_4 calculated using (a) SCAN, (b) SCAN+U, (c) r^{2}SCAN and (d) r^{2}SCAN+U.

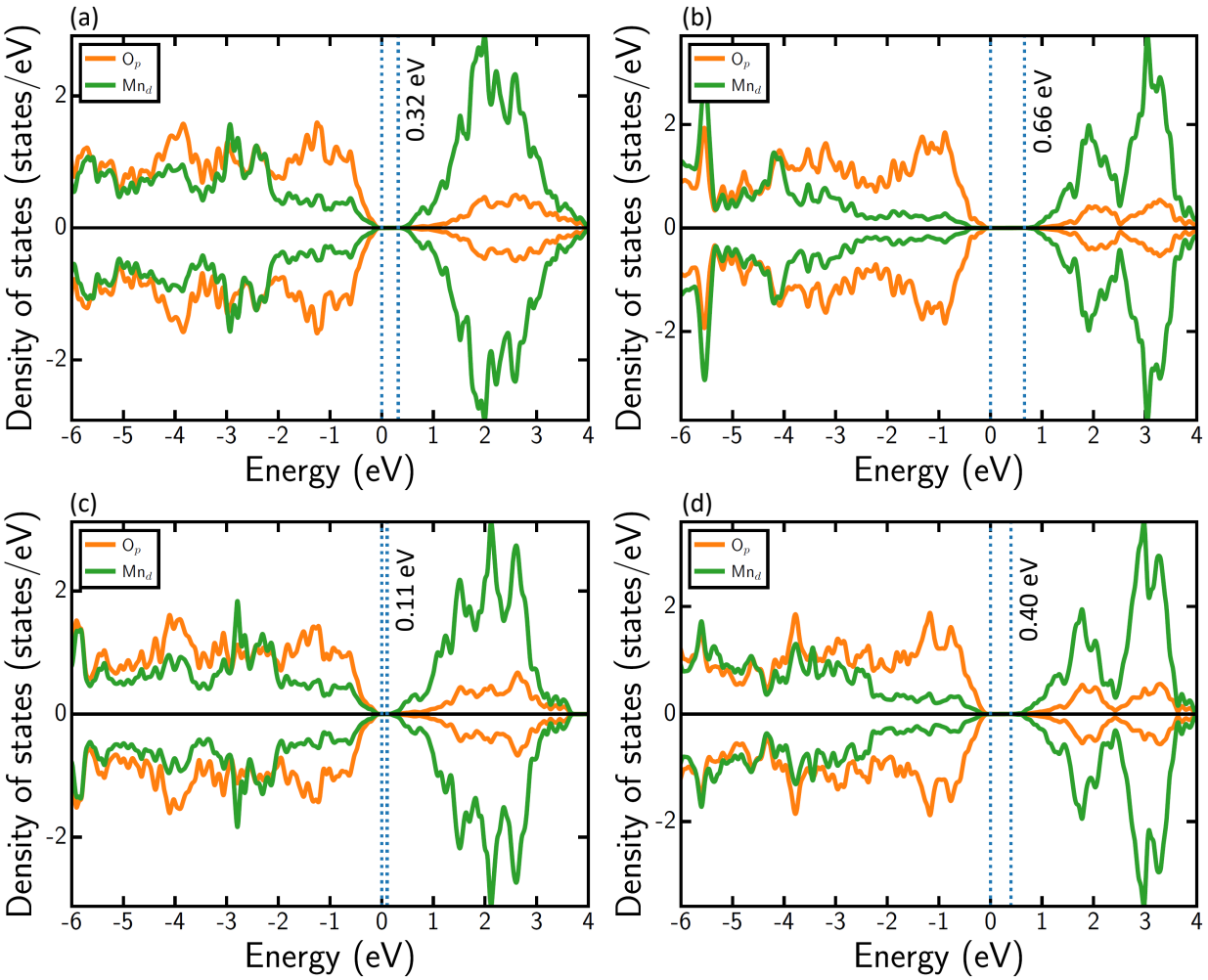

Figure S14: DOS plots for MnO_2 calculated using (a) SCAN, (b) SCAN+U, (c) r^{2}SCAN and (d) r^{2}SCAN+U.

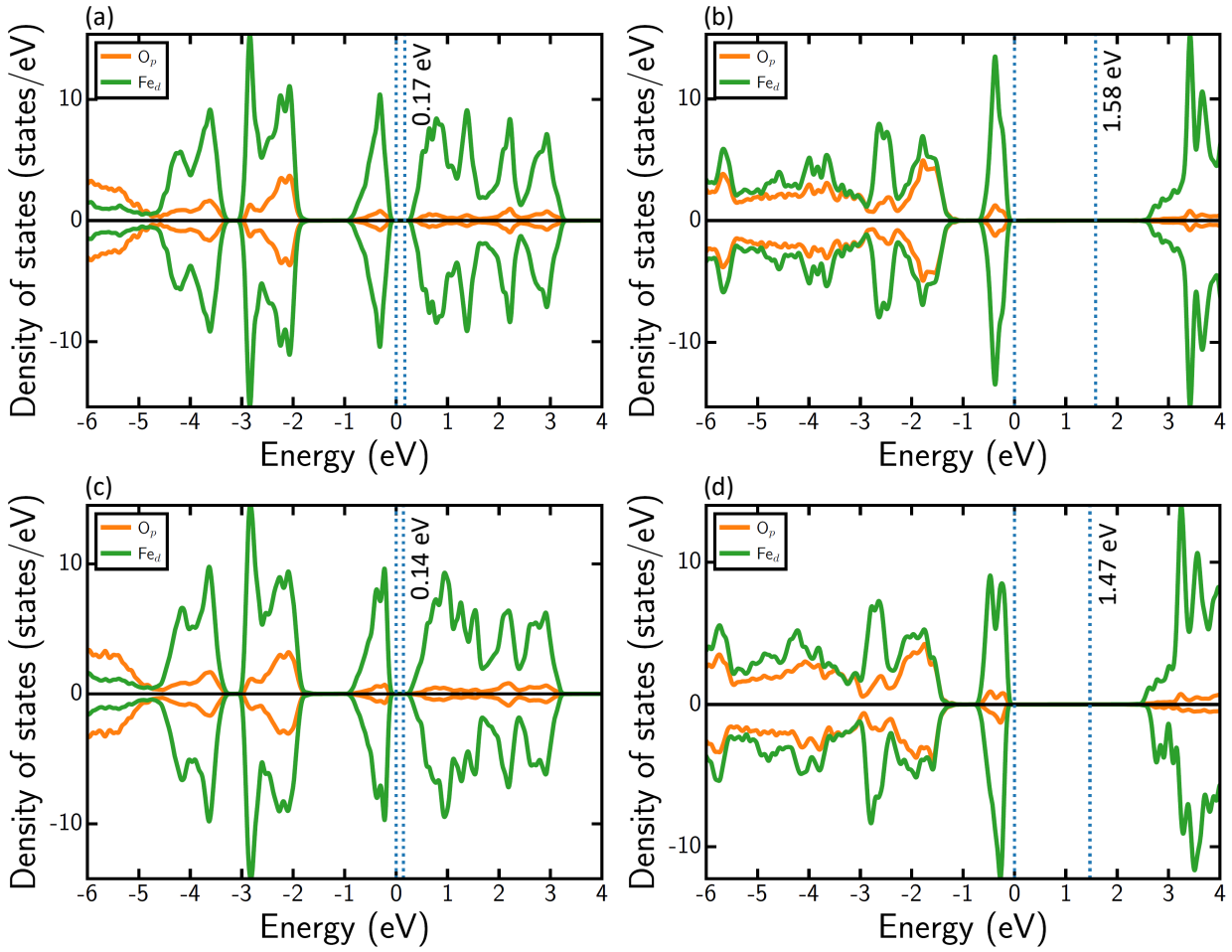

Figure S15: DOS plots for FeO calculated using (a) SCAN, (b) SCAN+U, (c) r^{2}SCAN and (d) r^{2}SCAN+U.

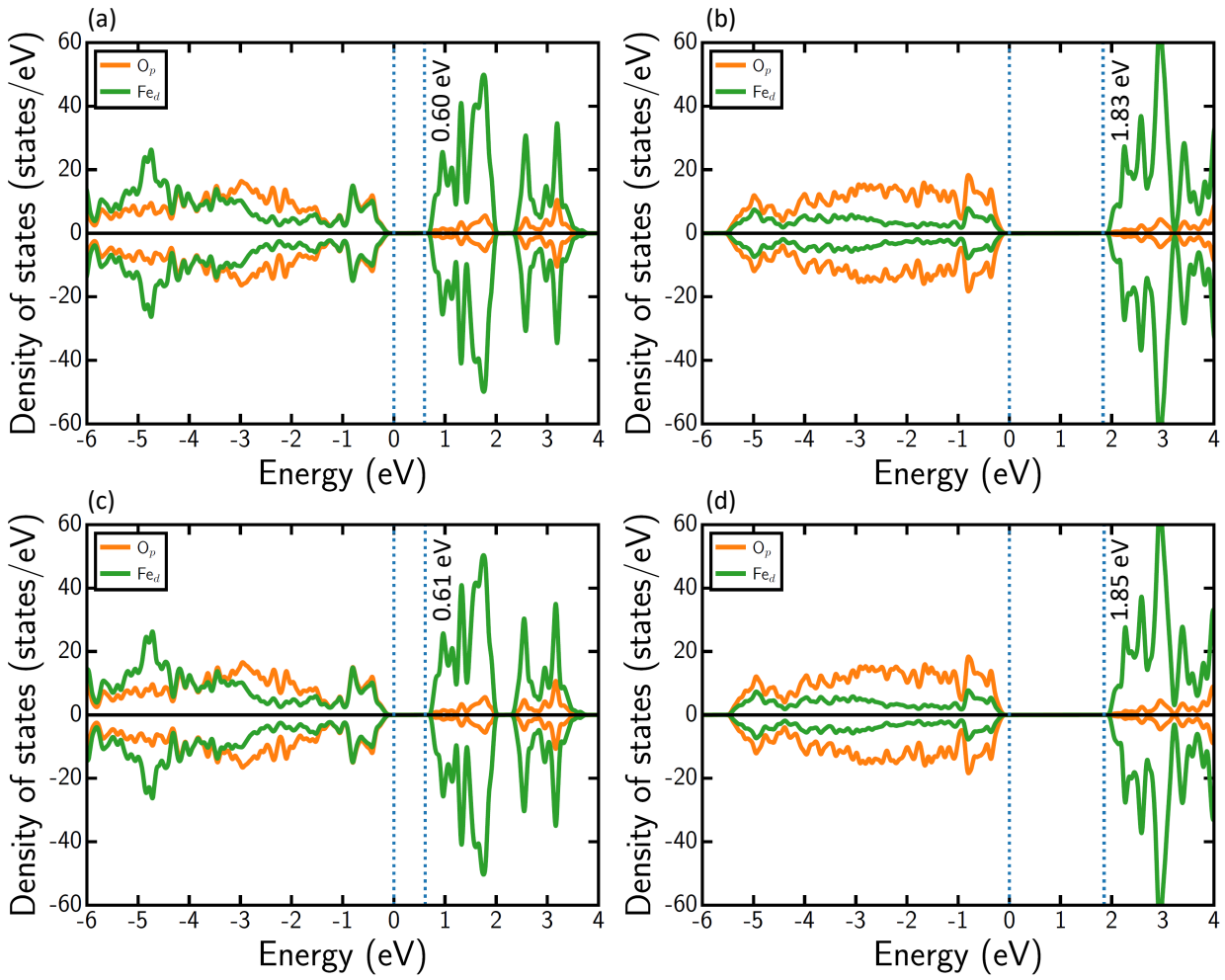

Figure S16: DOS plots for Fe_2O_3 calculated using (a) SCAN, (b) SCAN+U, (c) r^{2}SCAN and (d) r^{2}SCAN+U.

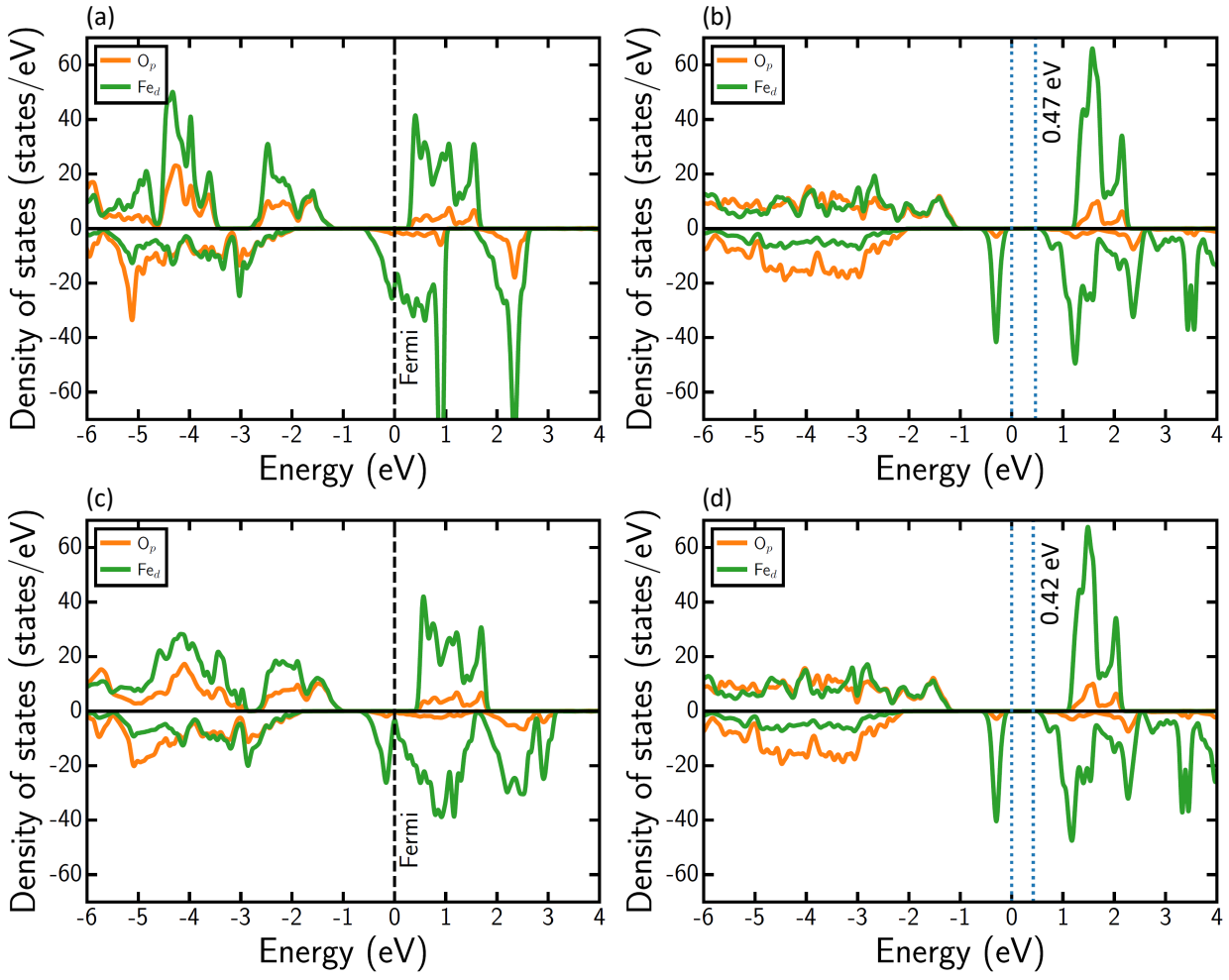

Figure S17: DOS plots for Fe_3O_4 calculated using (a) SCAN, (b) SCAN+U, (c) r^{2}SCAN and (d) r^{2}SCAN+U.

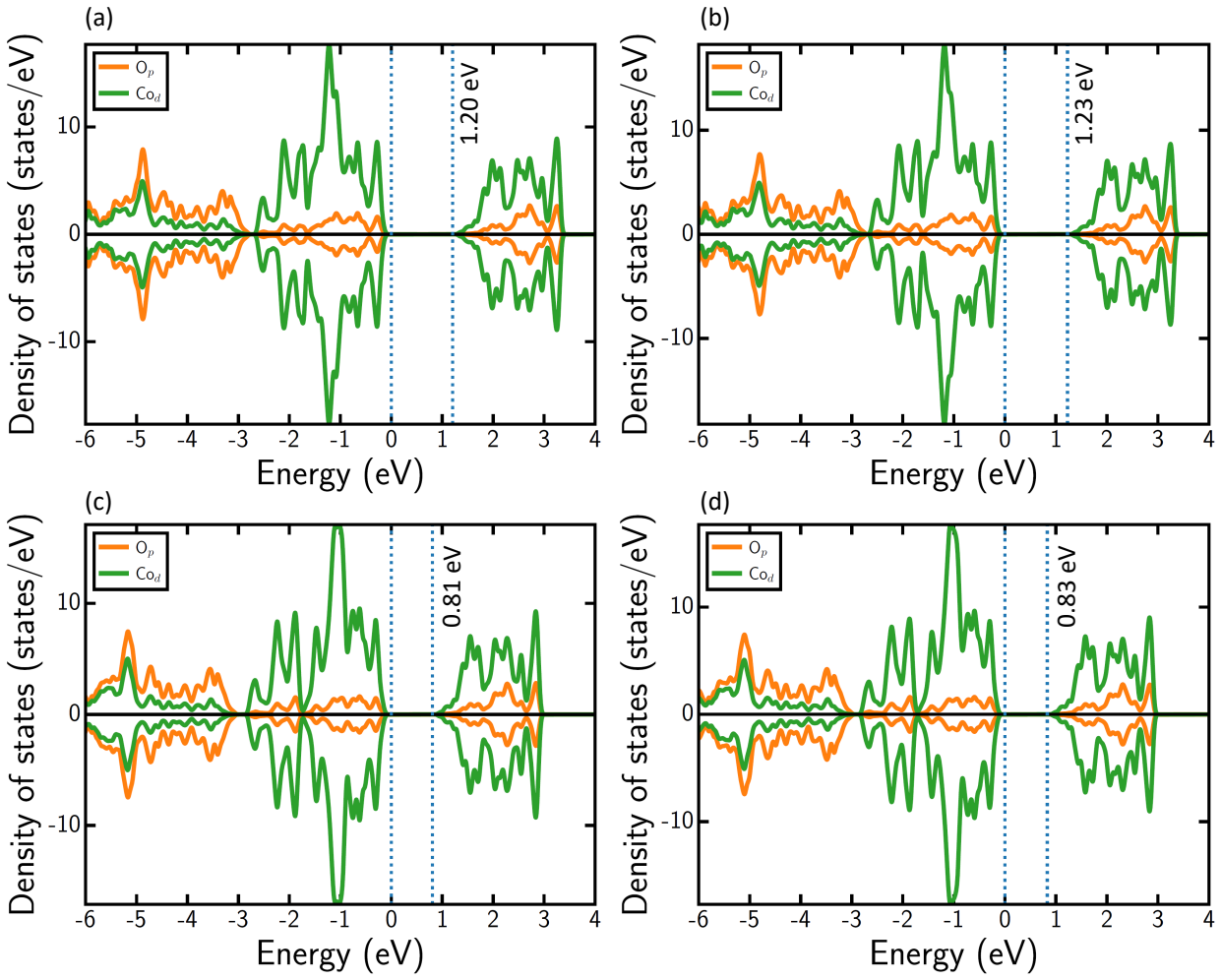

Figure S18: DOS plots for Co_3O_4 calculated using (a) SCAN, (b) SCAN+U, (c) r^{2}SCAN and (d) r^{2}SCAN+U.

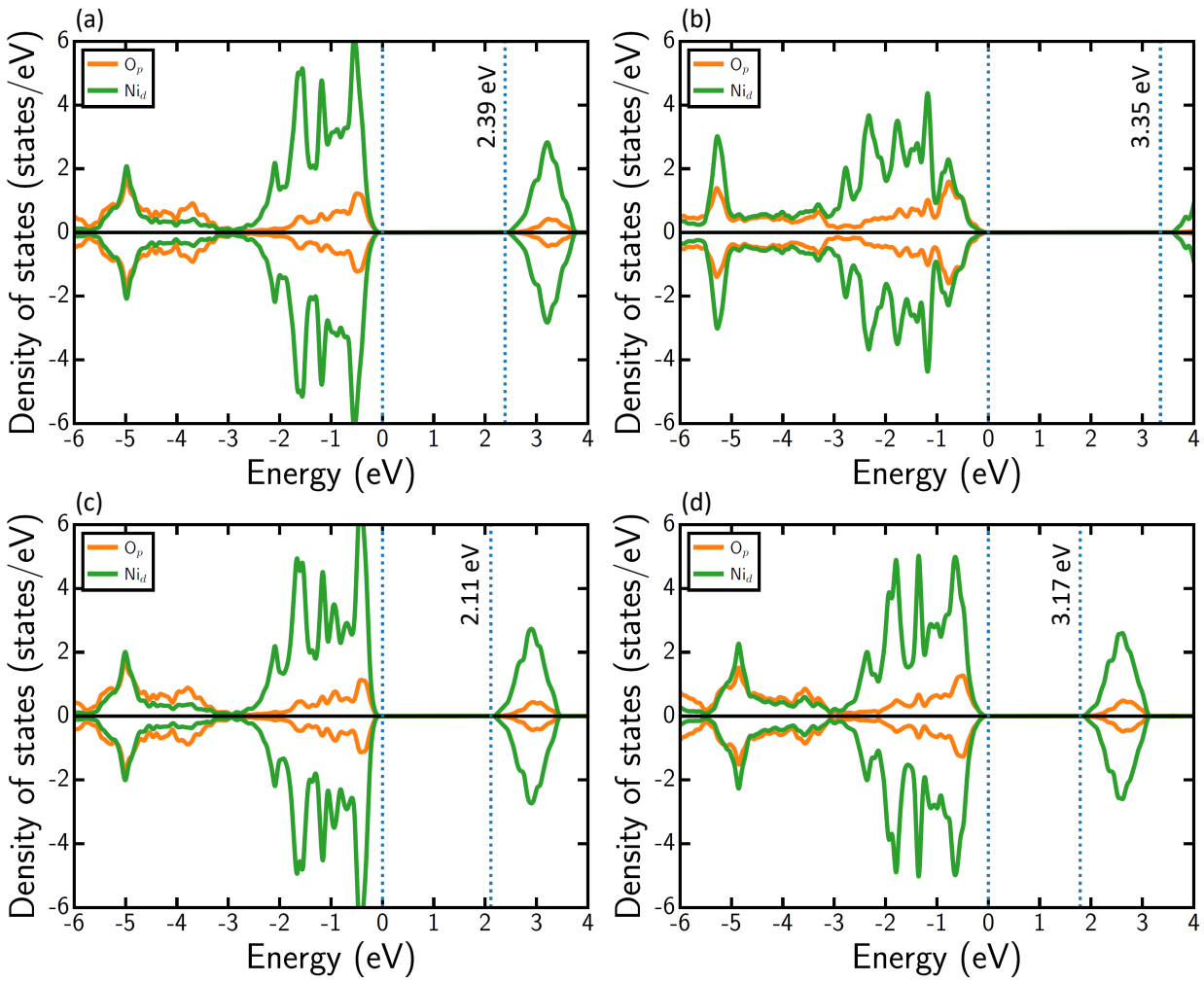

Figure S19: DOS plots for NiO calculated using (a) SCAN, (b) SCAN+U, (c) r^{2}SCAN and (d) r^{2}SCAN+U.

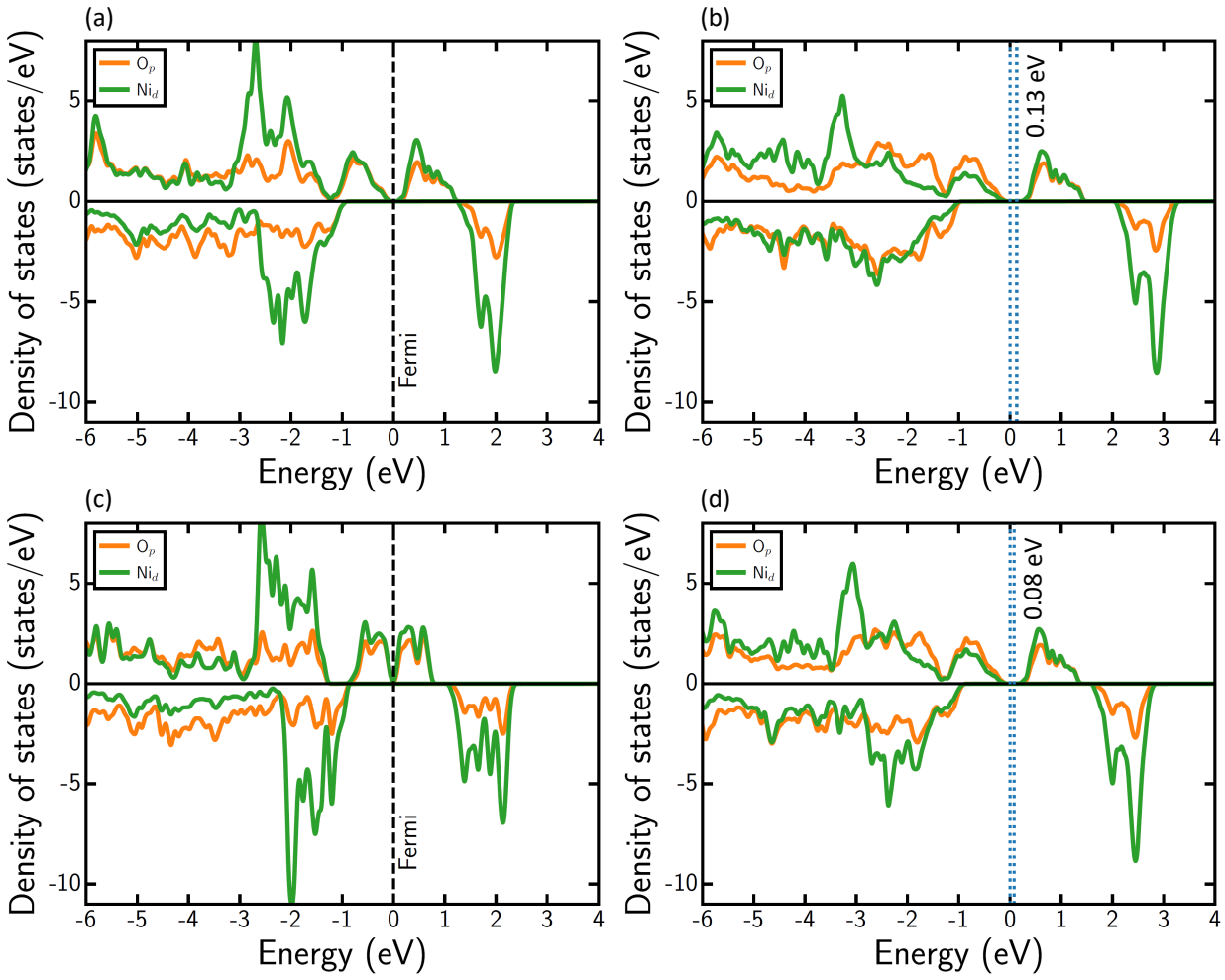

Figure S20: DOS plots for $LiNiO_2$ calculated using (a) SCAN, (b) SCAN+U, (c) r^{2}SCAN and (d) r^{2}SCAN+U.

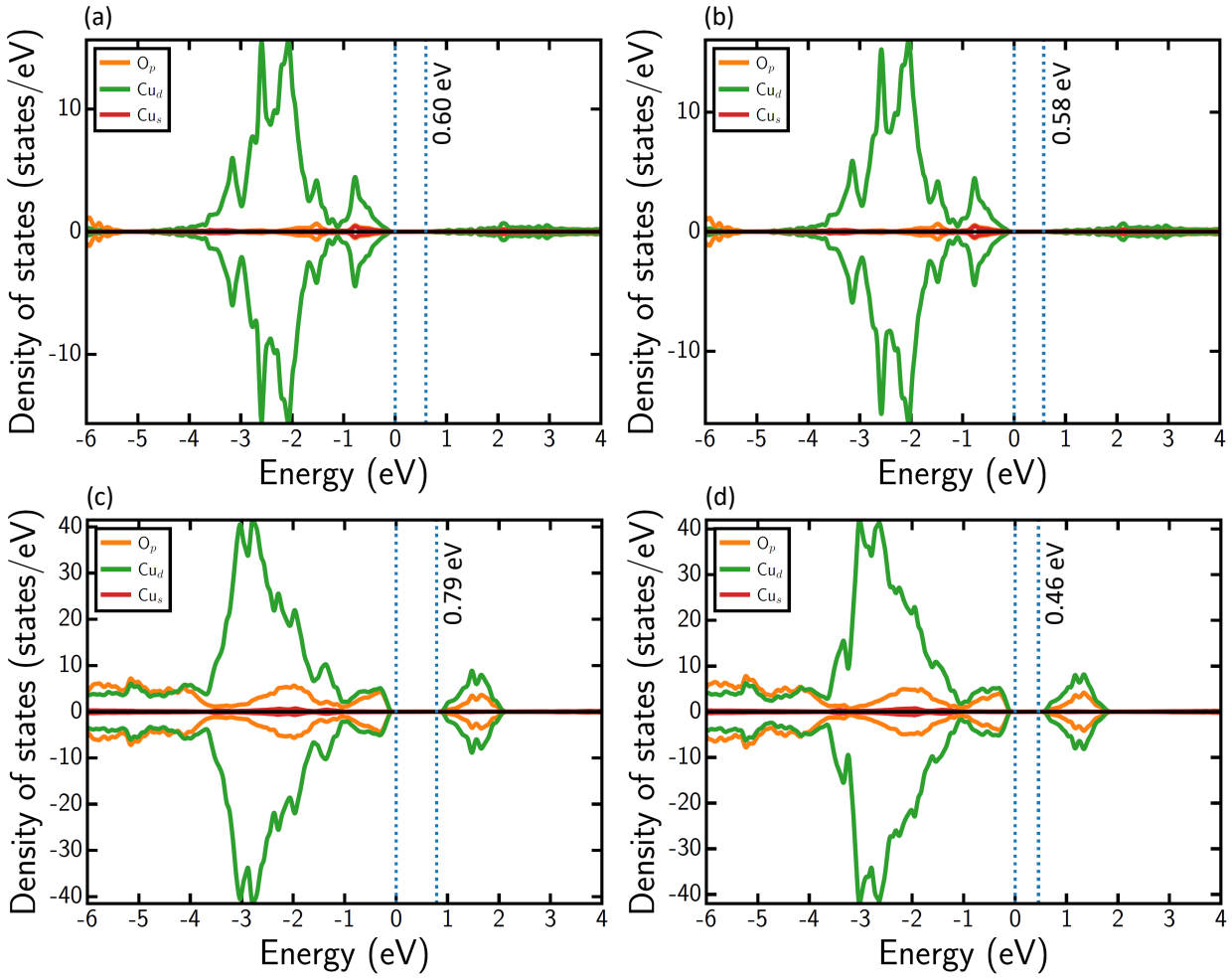

Figure S21: DOS plots for Cu_2O (panels a and b), and CuO (c and d), calculated using SCAN (panels a and c) and r^{2}SCAN (b and d).

References

(1) Baur, W. H. Rutile-Type Compounds. V. Refinement of MnO_2 and MgF_2. *Acta Crystallogr., Sect. B* **1976**, *32*, 2200.

(2) Kang, W.; Hybertsen, M. S. Quasiparticle and optical properties of rutile and anatase TiO 2. *Phys. Rev. B* **2010**, *82*, 085203.

(3) Coey, J.; Venkatesan, M. Half-metallic ferromagnetism: Example of CrO_2. *J. Appl. Phys.* **2002**, *91*, 8345–8350.

(4) Voinov, M. MnO2: structure and activity. *Electrochim. Acta* **1982**, *27*, 833–835.

(5) Porta, P.; Marezio, M.; Remeika, J.; Dernier, P. D. Chromium dioxide: High pressure synthesis and bond lengths. *Materials Research Bulletin* **1972**, *7*, 157–161.

(6) Regulski, M.; Przeniosło, R.; Sosnowska, I.; Hoffmann, J.-U. Incommensurate magnetic structure of β-MnO_2. *Phys. Rev. B* **2003**, *68*, 172401.

(7) Rogers, K. D. An X-ray diffraction study of semiconductor and metallic vanadium dioxide. *Powder Diffr.* **1993**, *8*, 240–244.

(8) Robinson, W. R. The crystal structures of Ti_2O_3, a semiconductor, and $(Ti_{0.900}V_{0.100})_2O_3$, a semimetal. *J. Solid State Chem.* **1974**, *9*, 255–260.

(9) Crawford, J. A.; Vest, R. W. Electrical conductivity of single-crystal Cr2O3. *Journal of Applied Physics* **1964**, *35*, 2413–2418.

(10) Brockhouse, B. N. Antiferromagnetic structure in Cr_2O_3. *J. Chem. Phys.* **1953**, *21*, 961–962.

(11) Abrahams, S. C. Magnetic and crystal structure of titanium sesquioxide. *Phys. Rev.* **1963**, *130*, 2230–2237.

(12) Loehman, R.; Rao, C. R.; Honig, J. M. Crystallography and defect chemistry of solid solutions of vanadium and titanium oxides. *J. Phys. Chem.* **1969**, *73*, 1781–1784.

(13) Rozier, P.; Ratuszna, A.; Galy, J. Comparative Structural and Electrical Studies of V_2O_3 and $V_{2-x}Ni_xO_3$ ($0<x<0.75$) Solid Solution. *Z. Anorg. Allg. Chem.* **2002**, *628*, 1236–1242.

(14) Ashkenazi, J.; Chuchem, T. Band structure of V_2O_3, and Ti_2O_3. *Phil. Mag.* **1975**, *32*, 763–785.

(15) Maslen, E. N.; Streltsov, V. A.; Streltsova, N. R.; Ishizawa, N. Synchrotron X-ray study of the electron density in α-Fe_2O_3. *Acta Crystallogr., Sect. B* **1994**, *50*, 435–441.

(16) Satoshi Sasaki, K. F.; Takeuchi, Y. X.Ray Determination of Electron Density Distributions in Oxides, MgO, MnO, CoO, and NiO, and Atomic Scattering Factors of their Constituent Atoms. *Proc. Jpn. Acad., Ser. B* **1979**, *55*, 43–48.

(17) Kuriyama, M.; Hosoya, S. X-ray measurement of scattering factors of manganese and oxygen atoms in manganous oxide. *J. Phys. Soc. Jpn.* **1962**, *17*, 1022–1029.

(18) Jauch, W.; Reehuis, M.; Bleif, H. J.; Kubanek, F.; Pattison, P. Crystallographic symmetry and magnetic structure of CoO. *Phys. Rev. B* **2001**, *64*.

(19) Shen, Z. X.; List, R. S.; Dessau, D. S.; Wells, B. O.; Jepsen, O.; Arko, A. J.; Barttlet, R.; Shih, C. K.; Parmigiani, F.; Huang, J. C.; Lindberg, P. A. Electronic structure of NiO: Correlation and band effects. *Phys. Rev. B* **1991**, *44*, 3604–3626.

(20) Fjellvåg, H.; Grønvold, F.; Stølen, S.; Hauback, B. On the crystallographic and magnetic structures of nearly stoichiometric iron monoxide. *J. Solid State Chem.* **1996**, *124*, 52–57.

(21) Hartmann, H.; Mässung, W. Elektrolyse in Phosphatschmelzen. IV. Über die Elektrolyse von Vanadin-, Niob-und Tantaloxyd in Phosphatschmelzen. *Z. Anorg. Allg. Chem.* **1951**, *266*, 98–104.

(22) Boucher, B.; Buhl, R.; Perrin, M. Magnetic structure of Mn_3O_4 by neutron diffraction. *J. Appl. Phys.* **1971**, *42*, 1615–1617.

(23) Gautam, G. S.; Carter, E. A. Evaluating transition metal oxides within DFT-SCAN and SCAN+U frameworks for solar thermochemical applications. *Phys. Rev. Mater.* **2018**, *2*, 095401.

(24) Abrahams, S.; Calhoun, B. The low-temperature transition in magnetite. *Acta Crystallographica* **1953**, *6*, 105–106.

(25) Iizumi, M.; Koetzle, T.; Shirane, G.; Chikazumi, S.; Matsui, M.; Todo, S. Structure of magnetite (Fe_3O_4) below the Verwey transition temperature. *Acta Crystallogr., Sect. B* **1982**, *38*, 2121–2133.

(26) Verwey, E. J. W. Electronic conduction of magnetite (Fe_3O_4) and its transition point at low temperatures. *Nature* **1939**, *144*, 327–328.

(27) Park, S. K.; Ishikawa, T.; Tokura, Y. Charge-gap formation upon the Verwey transition in Fe_3O_4. *Phys. Rev. B* **1998**, *58*, 3717.

(28) Smith, W. L.; Hobson, A. D. The structure of cobalt oxide, Co_3O_4. *Acta Crystallogr., Sect. B* **1973**, *29*, 362–363.

(29) Knop, O.; Reid, K.; Sutarno,; Nakagawa, Y. Chalkogenides of the transition elements. VI. X-Ray, neutron, and magnetic investigation of the spinels Co_30_4, $NiCo_2O_4$, Co_3S_4, and $NiCo_2S_4$. *Can. J. Chem.* **1968**, *46*, 3463.

(30) Roth, W. L. The magnetic structure of Co_3O_4. *J. Phys. Chem. Solids* **1964**, *25*, 1–10.

(31) Cockayne, E.; Levin, I.; Wu, H.; Llobet, A. Magnetic structure of bixbyite α-Mn_2O_3: A combined DFT+U and neutron diffraction study. *Phys. Rev. B* **2013**, *87*, 184413.

(32) Wang, M.; Navrotsky, A. Enthalpy of formation of $LiNiO_2$, $LiCoO_2$ and their solid solution, $LiNi_{1-x}Co_xO_2$. *Solid State Ion.* **2004**, *166*, 167–173.

(33) Enjalbert, R.; Galy, J. A refinement of the structure of V_2O_5. *Acta Crystallogr., Sect. C* **1986**, *42*, 1467–1469.

(34) Ghijsen, J.; Tjeng, L. H.; Elp, J. V.; Eskes, H.; Westerink, J.; Sawatzky, G. A.; Czyzyk, M. T. Electronic structure of Cu_2O and CuO. *Phys. Rev. B* **1988**, *38*, 11322–11330.

(35) Mittal, R.; Chaplot, S. L.; Mishra, S. K.; Bose, P. P. Inelastic neutron scattering and lattice dynamical calculation of negative thermal expansion compounds Cu_2O and Ag_2O. *Phys. Rev. B* **2007**, *75*, 174303.

(36) Long, O. Y.; Gautam, G. S.; Carter, E. A. Evaluating optimal U for $3d$ transition-metal oxides within the SCAN+U framework. *Phys. Rev. Mater.* **2020**, *4*, 045401.

(37) Moon, R. M.; Riste, T.; Koehler, W. C.; Abrahams, S. C. Absence of Antiferromagnetism in Ti_2O_3. *J. Appl. Phys.* **1969**, *40*, 1445–1447.

(38) Uchida, M.; Fujioka, J.; Onose, Y.; Tokura, Y. Charge Dynamics in Thermally and Doping Induced Insulator-Metal Transitions of $(Ti_{1-x}V_x)_2O_3$. *Phys. Rev. Lett.* **2008**, *101*, 066406.

(39) Serpone, N. Is the band gap of pristine TiO_2 narrowed by anion-and cation-doping of titanium dioxide in second-generation photocatalysts? *J. Phys. Chem. B* **2006**, *110*, 24287–24293.

(40) Moon, R. M. Antiferromagnetism in V_2O_3. *J. Appl. Phys.* **1970**, *41*, 883–883.

(41) Shin, S.; Tezuka, Y.; Kinoshita, T.; Kakizaki, A.; Ishii, T.; Ueda, Y.; Jang, W.; Takei, H.; Chiba, Y.; Ishigame, M. Observation of local magnetic moments in the Mott transition of V_2O_3 by means of 3s photoemission. *Phys. Rev. B* **1992**, *46*, 9224–9227.

(42) Shin, S.; Suga, S.; Taniguchi, M.; Fujisawa, M.; Kanzaki, H.; Fujimori, A.; Daimon, H.; Ueda, Y.; Kosuge, K.; Kachi, S. Vacuum-ultraviolet reflectance and photoemission study of the metal-insulator phase transitions in VO_2, V_6O_{13}, and V_2O_3. *Phys. Rev. B* **1990**, *41*, 4993–5009.

(43) Leroux-Hugon, P.; Paquet, D. Magnetic Susceptibility in the Insulating And Metallic Phases of VO_2: The Contribution of Electron-Electron AND Electron-Lattice Interactions. *J.Phys. Colloq.* **1980**, *41*, C5–67–C5–70.

(44) Kumar, A.; Singh, P.; Kulkarni, N.; Kaur, D. Structural and optical studies of nanocrystalline V_2O_5 thin films. *Thin Solid Films* **2008**, *516*, 912–918.

(45) Corliss, L. M.; Hastings, J. M.; Nathans, R.; Shirane, G. Magnetic structure of Cr_2O_3. *J. Appl. Phys.* **1965**, *36*, 1099–1100.

(46) Abdullah, M. M.; Rajab, F. M.; Al-Abbas, S. M. Structural and optical characterization of Cr_2O_3 nanostructures: Evaluation of its dielectric properties. *AIP Adv.* **2014**, *4*, 027121.

(47) Misho, R. H.; Murad, W. A.; Fattahallah, G. H. Preparation and optical properties of thin films of CrO_3 and Cr_2O_3 prepared by the method of chemical spray pyrolysis. *Thin Solid Films* **1989**, *169*, 235–239.

(48) Cheetham, A. K.; Hope, D. A. O. Magnetic ordering and exchange effects in the antiferromagnetic solid solutions $Mn_xNi_{1-x}O$. *Phys. Rev. B* **1983**, *27*, 6964–6967.

(49) Messick, L.; Walker, W.; Glosser, R. Direct and temperature-modulated reflectance spectra of MnO, CoO, and NiO. *Phys. Rev. B* **1972**, *6*, 3941–3949.

(50) Jensen, G. B.; Nielsen, O. The magnetic structure of Mn_3O_4 Hausmannite between 4.7K and Neel point, 41K. *J. Solid State Phys.* **1974**, *7*, 409.

(51) Xu, H. Y.; Le Xu, S.; Li, X. D.; Wang, H.; Yan, H. Chemical bath deposition of hausmannite Mn_3O_4 thin films. *Appl. Surf. Sci.* **2006**, *252*, 4091–4096.

(52) Regulski, M.; Przeniosło, R.; Sosnowska, I.; Hohlwein, D.; Schneider, R. Neutron diffraction study of the magnetic structure of α-Mn_2O_3. *J. Alloys Compd.* **2004**, *362*, 236–240.

(53) Rahaman, H.; Laha, R. M.; Maiti, D. K.; Ghosh, S. K. Fabrication of Mn_2O_3 nanorods: an efficient catalyst for selective transformation of alcohols to aldehydes. *RSC Adv.* **2015**, *5*, 33923–33929.

(54) Javed, Q.-u.-a.; Feng-Ping, W.; Rafique, M. Y.; Toufiq, A. M.; Iqbal, M. Z. Canted antiferromagnetic and optical properties of nanostructures of Mn_2O_3 prepared by hydrothermal synthesis. *Chin. Phys. B* **2012**, *21*, 117311.

(55) Druilhe, R.; Suchet, J. P. Electron transport in CrO_2 and $Mn_xCr_{1-x}O_2$. *Czechoslov. J. Phys. B* **1967**, *17*, 337–346.

(56) Islam, A. K. M.; Islam, R.; Khan, K. A. Studies on the thermoelectric effect in semiconducting MnO_2 thin films. *J. Mater. Sci.: Mater. Electron.* **2005**, *16*, 203–207.

(57) Battle, P. D.; Cheetham, A. K. The magnetic structure of non-stoichiometric ferrous oxide. *J. Solid State Phys.* **1979**, *12*, 337.

(58) Roth, W. L. Magnetic structures of MnO, FeO, CoO, and NiO. *Phys. Rev.* **1958**, *110*, 1333–1341.

(59) Bowen, H. K.; Adler, D.; Auker, B. H. Electrical and optical properties of FeO. *J. Solid State Chem.* **1975**, *12*, 355–359.

(60) Wright, J. P.; Attfield, J. P.; Radaelli, P. G. Charge ordered structure of magnetite Fe_3O_4 below the Verwey transition. *Phys. Rev. B* **2002**, *66*, 214422.

(61) Shull, C. G.; Strauser, W. A.; Wollan, E. O. Neutron diffraction by paramagnetic and antiferromagnetic substances. *Phys. Rev.* **1951**, *83*, 333–345.

(62) Droubay, T.; Rosso, K. M.; Heald, S. M.; Mccready, D. E.; Wang, C. M.; Chambers, S. A. Structure, magnetism, and conductivity in epitaxial Ti-doped α-Fe_2O_3 hematite: Experiment and density functional theory calculations. *Phys. Rev. B* **2007**, *75*, 104412.

(63) Khan, D. C.; Erickson, R. A. Magnetic form factor of Co^{++} ion in cobaltous oxide. *Phys. Rev. B* **1970**, *1*, 2243–2249.

(64) Van Elp, J.; Wieland, J. L.; Eskes, H.; Kuiper, P.; Sawatzky, G. A.; De Groot, F. M. F.; Turner, T. S. Electronic structure of CoO, Li-doped CoO, and $LiCoO_2$. *Phys. Rev. B* **1991**, *44*, 6090–6103.

(65) Wei, P.; Qi, Z. Q. Insulating gap in the transition-metal oxides: A calculation using the local-spin-density approximation with the on-site Coulomb U correlation correction. *Phys. Rev. B* **1994**, *49*, 10864–10868.

(66) Anisimov, V. I.; Zaanen, J.; Andersen, O. K. Band theory and Mott insulators: Hubbard U instead of Stoner I. *Phys. Rev. B* **1991**, *44*, 943–954.

(67) Sawatzky, G. A.; Allen, J. W. Magnitude and origin of the band gap in NiO. *Phys. Rev. Lett.* **1984**, *53*, 2339–2342.

(68) Reynaud, F.; Ghorayeb, A. M.; Ksari, Y.; Menguy, N.; Stepanov, A.; Delmas, C. On the 240 K anomaly in the magnetic properties of $LiNiO_2$. *Eur. Phys. J. B* **2000**, *14*, 83–90.

(69) Reynaud, F.; Mertz, D.; Celestini, F.; Debierre, J.-M.; Ghorayeb, A. M.; Simon, P.; Stepanov, A.; Voiron, J.; Delmas, C. Orbital frustration at the origin of the magnetic behavior in $LiNiO_2$. *Phys. Rev. Lett.* **2001**, *86*, 3638–3641.

(70) Zhang, L.; McMillon, L.; McNatt, J. Gas-dependent bandgap and electrical conductivity of Cu_2O thin films. *Sol. Energy Mater. Sol. Cells* **2013**, *108*, 230–234.

(71) Yang, B. X.; Tranquada, J. M.; Shirane, G. Neutron scattering studies of the magnetic structure of cupric oxide. *Phys. Rev. B* **1988**, *38*, 174–178.